Mg$_{12}$O$_{12}$ and Be$_{12}$O$_{12}$ Nanocages as Sorbents and Sensors for H$_2$S and SO$_2$ Gases: A Theoretical Approach

H. M. Badran [1], Kh. M. Eid [2,3], Sotirios Baskoutas [4] and H. Y. Ammar [1,*]

[1] Physics Department, College of Science and Arts, Najran University, Najran 11001, Saudi Arabia; hmbadran@nu.edu.sa

[2] Physics Department, Faculty of Education, Ain Shams University, Cairo 11566, Egypt; khmeid@yahoo.com

[3] Department of Physics, College of Science and Arts, Qassim University, Albukayriyah 52725, Saudi Arabia

[4] Department of Materials Science, University of Patras, 26504 Patras, Greece; bask@upatras.gr

[*] Correspondence: hyammar@hotmail.com

Abstract: Theoretical calculations based on the Density Functional Theory (DFT) have been performed to investigate the interaction of H$_2$S as well SO$_2$ gaseous molecules at the surfaces of Be$_{12}$O$_{12}$ and Mg$_{12}$O$_{12}$ nano-cages. The results show that a Mg$_{12}$O$_{12}$ nano-cage is a better sorbent than a Be$_{12}$O$_{12}$ nano-cage for the considered gases. Moreover, the ability of SO$_2$ gas to be adsorbed is higher than that of H$_2$S gas. The HOMO–LUMO gap (E$_g$) of Be$_{12}$O$_{12}$ nano-cage is more sensitive to SO$_2$ than H$_2$S adsorption, while the E$_g$ value of Mg$_{12}$O$_{12}$ nano-cage reveals higher sensitivity to H$_2$S than SO$_2$ adsorption. The molecular dynamic calculations show that the H$_2$S molecule cannot be retained at the surface of a Be$_{12}$O$_{12}$ nano-cage within 300–700 K and cannot be retained on a Mg$_{12}$O$_{12}$ nano-cage at 700 K, while the SO$_2$ molecule can be retained at the surfaces of Be$_{12}$O$_{12}$ and Mg$_{12}$O$_{12}$ nano-cages up to 700 K. Moreover, the thermodynamic calculations indicate that the reactions between H$_2$S as well SO$_2$ with Be$_{12}$O$_{12}$ and Mg$_{12}$O$_{12}$ nano-cages are exothermic. Our results suggest that we can use Be$_{12}$O$_{12}$ and Mg$_{12}$O$_{12}$ nano-cages as sorbents as well as sensors for H$_2$S and SO$_2$ gases.

Keywords: adsorption of H$_2$S and SO$_2$; BeO and MgO nano-cages; density functional theory; thermodynamics; molecular dynamics

1. Introduction

Recently, great efforts have been made to develop novel gas sensors and detectors as well as gas-removing materials. This is to control the pollutant gases broadly produced from industrial activities and burning fuel, etc. The toxic H$_2$S and SO$_2$ gases are produced as byproducts from SF6 decomposition, which is widely used as an insulating gas in high-voltage transformers and circuit breakers [1–4]. H$_2$S is mostly found in crude petroleum, natural gas, and coal gasification. In addition, some organic materials decompose, releasing H$_2$S [5–7]. H$_2$S is also released in many industries such as the paper industry and bio-mass fermenters [7,8]. The combustion of sulfur-containing fossil fuels releases SO$_2$ into the air, and SO$_2$ is naturally released as a byproduct of volcanic activity [9,10]. The H$_2$S as well SO$_2$ gases pose several hazards to the environment and human health. H$_2$S exposure leads to coughing, eye irritation, and a runny nose, harms the nervous system by killing the neurons and may cause death [11,12]. Moreover, H$_2$S is a corrosive gas and has devastating impacts on industrial catalysts [7,8]. SO$_2$ interacts with the air resulting in acidic rain which causes the corrosion of metals and disintegration of buildings [9,10]. Furthermore, SO$_2$ causes skin burning, eye irritation and respiratory system inflammation, and may cause death [7,13–15]. Therefore, several attempts have been made to utilize many materials as sorbents and detectors for H$_2$S and SO$_2$ gases, such as fullerene-like gallium

nitride [16], CuO(111) surface [17], pristine graphene and graphene oxide [18], NH-decorated graphene [8], activated carbon, [19,20], pillared clays [21], zeolites [22], p-CuO/n-ZnO Heterojunction [23], Cu (100) and Au (100) surfaces [24,25], Cu doped $MoSe_2$ [12], monolayer Janus MoSSe [26], aza-macrocycle [27], Cu-modified and Cu-embedded WSe_2 monolayers [28], porous N_4O_4-donor macrocyclic Schiff base [29] and MgO (100) surfaces [10].

Metal oxides have a significant consideration due to their several applications. They are usually utilized as substrates for epitaxial growth of multilayers and clusters, catalytic processes, hydrogen storage materials, sensors and sorbent materials [10,30–34]. Recently, nano-structures have been frequently utilized as gas detectors and sorbents due to their appropriate features such as their tiny size, precision, and reactivity [35–37].

Furthermore, Shamlouei et al. reported that nanocages with a $X_{12}Y_{12}$ structure are the most stable among $(XY)_n$ nano-cages [38]. Ren et al. [39] have investigated $(BeO)_N$ clusters and found that $Be_{12}O_{12}$ is one of the most feasible nano-cages. Ziemann and Castleman [40] have proven that a $Mg_{12}O_{12}$ nano-cage displays unique stability among $(MgO)_n$, $n \leq$ 90 nano-structures. The Mg-O bond in $Mg_{12}O_{12}$ nano-cages has an ionic character [38], while the Be-O bond has ionic and covalent characters [41], therefore one can expect different applications for $Be_{12}O_{12}$ and $Mg_{12}O_{12}$ nano-cages. $Be_{12}O_{12}$ and $Mg_{12}O_{12}$ have several applications; for instance, $Be_{12}O_{12}$ has been utilized as a catalyst to convert CH_4 into CH_3OH [42], an electro-conductive sensor for sulfur mustard [43], and a detector and sorbent for Mercaptopyridine [44], and $Be_{12}O_{12}$ and $Mg_{12}O_{12}$ have been utilized for hydrogen storage applications [45,46], detection and adsorption of Tabun [47]

According to our knowledge, the interaction of H_2S and SO_2 gases at the surfaces of $Be_{12}O_{12}$ and $Mg_{12}O_{12}$ nano-cages has not been investigated yet. Hence, the present work aims to shed light on the characteristics of the interaction of H_2S and SO_2 with $Be_{12}O_{12}$ and $Mg_{12}O_{12}$ nano-cages for adsorption and sensing applications using DFT calculations.

2. Methods

To investigate the adsorption characteristics of H_2S and SO_2 molecules onto $Be_{12}O_{12}$ and $Mg_{12}O_{12}$ nano-cages, DFT and DFT-D3 methods [48] are used at the B3LYP/6-31G(d,p) level. D3 is a version of Grimme's dispersion [49]. B3 is Becke's three-parameter exchange functional [50] and LYP is the correlation functional of Lee, Yang and Parr [51,52]. A geometrical optimization without any restriction is performed for the free gaseous molecules, bare nano-cages and gas/nano-cage complexes. The ionization potential (IP) is calculated as [10,37]:

$$IP = E_{nano-cage^+} - E_{nano-cage} \tag{1}$$

where $E_{nano-cage^+}$ is the energy of the nano-cage with one electron lost at the same geometrical structure of the neutrally charged nano-cage. The chemical potential (μ), hardness (η) and electrophilicity (ω) are calculated as [53,54]:

$$\mu \approx -\frac{1}{2}\left(E_{HOMO} + E_{LUMO}\right) \tag{2}$$

$$\eta \approx \frac{1}{2}\left(E_{LUMO} - E_{HOMO}\right) \tag{3}$$

$$\omega \approx \frac{\mu^2}{2\eta} \tag{4}$$

Molecular dynamic simulations via the Atom Centered Density Matrix Propagation molecular dynamics model (ADMP) as implemented in Gaussian 09 package are achieved for the investigated nano-cages and gas/nano-cage complexes.

The adsorption energy (E_{ads}) and the corrected adsorption energy (E_{ads}^{corr}) with basis set superposition error (BSSE) have been estimated as [55]:

$$E_{ads} = E_{gas/nano-cage} - (E_{gas} + E_{nano-cage}) \tag{5}$$

$$E_{ads}^{corr} = E_{ads} + E_{BSSE} \tag{6}$$

where $E_{gas/nano-cage}$, E_{gas}, and $E_{nano-cage}$ are the energies of gas/nano-cage complexes, free gas molecules, and bare nano-cages, respectively. The charge density difference ($\Delta\rho$) for the complexes is computed as:

$$\Delta\rho = \rho_{gas/nano-cage} - (\rho_{gas} + \rho_{nano-cage}) \tag{7}$$

where $\rho_{gas/nano-cage}$, ρ_{gas}, and $\rho_{nano-cage}$ are the charge densities for gas/nano-cage complexes, free gas molecules, and bare nano-cages, respectively.

Thermodynamic calculations are performed via vibrational calculations to predict enthalpies as well free energies for the considered gases, nano-cages, and gas-cages complexes. Enthalpy difference (ΔH) and free energy difference (ΔG) for gas/nano-cage complexes are evaluated as [56]:

$$\Delta H = H_{gas/nano-cage} - (H_{gas} + H_{nano-cage}) \tag{8}$$

where $H_{gas/nano-cage}$, $H_{nano-cage}$, and H_{gas} are the enthalpies for gas/nano-cage complexes, bare nano-cages and free gas molecules, respectively.

$$\Delta G = G_{gas/nano-cage} - (G_{gas} + G_{nano-cage}) \tag{9}$$

where $G_{gas/nano-cage}$, $G_{nano-cage}$, and G_{gas} are the free energies for gas/nano-cage complexes, bare nano-cages, and free gas molecules, respectively.

All the calculations have been carried out by Gaussian 09 program package [57]. GaussSum3.0 program is used to visualize the densities of states (DOS) [58]. Atomic charges are calculated for the considered structures via full natural bond orbital (NBO) analyses by using NBO version 3.1 [59].

3. Results and Discussions

3.1. Structural and Electronic Properties of $Be_{12}O_{12}$ and $Mg_{12}O_{12}$

The optimized structures for the scrutinized adsorbed gases H_2S and SO_2, as well the adsorbent nano-cages $Be_{12}O_{12}$ and $Mg_{12}O_{12}$, are shown in Figure 1.

For H_2S gas, the S-H bond length and the H-S-H angle are 1.35 Å and 92.52°, respectively, while for SO_2 gas, the S-O bond length and the O-S-O angle are 1.46 Å and 119.16°, respectively, in good agreement with previous studies [10,29]. $Be_{12}O_{12}$, as well $Mg_{12}O_{12}$ nano-cages are constructed of eight hexagonal and six tetragonal rings. It is noticed that all the metallic (Be and Mg) and O sites are identical. These nano-cages have two metal–oxygen bond types. They are denoted as d_1 and d_2 in Figure 1, where d_1 shares a hexagon ring and a tetragon ring while d_2 shares two hexagon rings. The d_1 values are 1.58 and 1.95 Å, whereas the d_2 values are 1.52 and 1.90 Å for $Be_{12}O_{12}$ and $Mg_{12}O_{12}$, respectively, match well with the previous studies [39,60–63]. Table 1 represents the electronic properties of $Be_{12}O_{12}$ and $Mg_{12}O_{12}$ nano-cages.

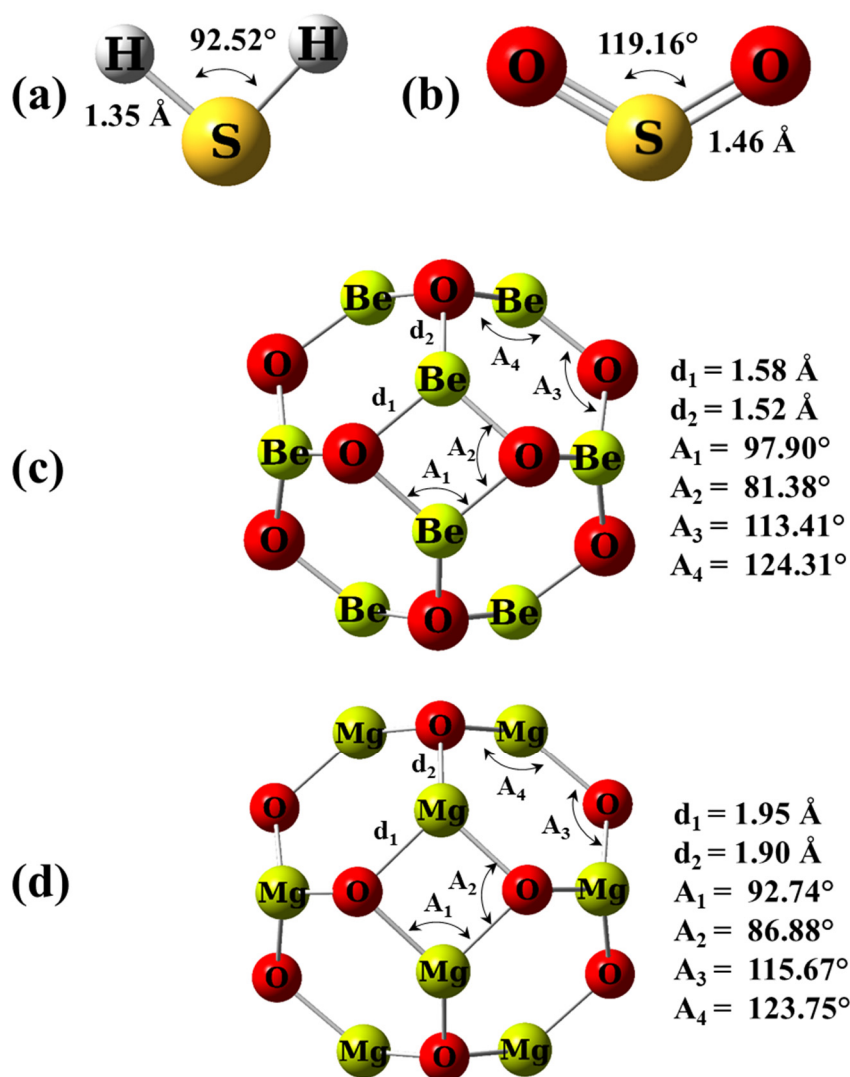**Figure 1.** The optimized structures for (**a**) free H_2S gas, (**b**) free SO_2 gas, (**c**) $Be_{12}O_{12}$, and (**d**) $Mg_{12}O_{12}$ nano-cages.

Table 1. Electronic properties of $Be_{12}O_{12}$ and $Mg_{12}O_{12}$ nano-cages. HOMO and LUMO energy levels (eV), HOMO- LUMO gap (E_g, eV), ionization potential (IP, eV), NBO charges (Q, e), chemical potential (μ, eV), hardness (η, eV), electrophilicity (ω, eV), and dipole moment (D, Debye).

	$Be_{12}O_{12}$		$Mg_{12}O_{12}$	
	Present Study	**Previous Studies**	**Present Study**	**Previous Studies**
HOMO	−8.62	−8.62 [57]	−6.59	−6.58 [57], −6.57 [58], −6.60 [38], −6.58 [59], −6.74 [30,31], −6.53 [10]
LUMO	−0.79	−1.07 [57]	−1.75	−1.78 [57], −1.71 [58], −1.80 [38], −1.72 [59]
E_g	7.83	8.29 [43], 7.41 [45],	4.84	4.87 [43], 4.83 [45],

		7.55 [57]	4.79 [57], 4.86 [58,59], 4.78 [30,31]
IP	10.27	7.98	
Q_M	1.19	1.44	
Q_O	−1.19	−1.44	
μ	−4.71	−4.17	−4.14 [58]
η	3.92	2.42	
ω	2.83	3.60	
D	0.00	0.01	0.01 [58], 0.00 [38], 0.07 [59]

M= Be and Mg.

The HOMO–LUMO energy gap (E_g) values for $Be_{12}O_{12}$ and $Mg_{12}O_{12}$ are 7.829 and 4.839 eV while the ionization potential (IP) values are 10.273 and 7.983 eV, respectively, in good agreement with the previous studies [10,30,31,39,44,60–63]. The lower IP value for the $Mg_{12}O_{12}$ nano-cage suggests its higher ability to donate electrons than the $Be_{12}O_{12}$ nano-cage. The atomic charges for the investigated nano-cage are calculated via natural bond orbital (NBO) analysis. For $Be_{12}O_{12}$, the atomic charges for Be and O sites are 1.186 and -1.186 e, while for $Mg_{12}O_{12}$, the atomic charges for Mg and O sites are 1.442 and −1.442 e, respectively. In other words, the charge polarization for the Mg-O bond is greater than that for the Be-O bond; therefore, the $Mg_{12}O_{12}$ is expected to be more reactive than $Be_{12}O_{12}$. This matches the calculated E_g, IP, η, and ω values, where the higher chemical stability and consequently lower reactivity for a molecule are marked by wide E_g, large IP, η, and low ω values [64–67]. Figure 2 illustrates the molecular electrostatic potential (MESP) for H_2S, SO_2, $Be_{12}O_{12}$, and $Mg_{12}O_{12}$.

It is clear that the S atom is surrounded by negative and positive electrostatic potentials for H_2S and SO_2 molecules, respectively. Furthermore, the MESP around the SO_2 molecule is extended in space more than that of the H_2S molecule.

For $Be_{12}O_{12}$ and $Mg_{12}O_{12}$ nano-cages, the O atoms and the metallic atoms are surrounded by negative and positive electrostatic potentials, respectively. In addition, the MESP of $Mg_{12}O_{12}$ is more extended around the nano-cage than that of the $Be_{12}O_{12}$ nano-cage. This is due to the higher charge polarization of $Mg_{12}O_{12}$. Therefore, it is expected that the S atoms of H_2S and SO_2 tend to be attracted to the metallic sites and oxygen sites of the nano-cages, respectively. Furthermore, the electric dipole moment (D) of $Be_{12}O_{12}$ and $Mg_{12}O_{12}$ nano-cages are 0.001 and 0.010 Debye, respectively. The low D values are owing to the uniform charge distribution on the nano-cages.

Molecular dynamic (MD) simulations examine the stability of the considered nano-cages at 300, 500, 700 K for a total time of 500 fs. Figure 3 depicts the fluctuation of the potential energy versus the time and the nano-cage geometric configuration at the end of the period.
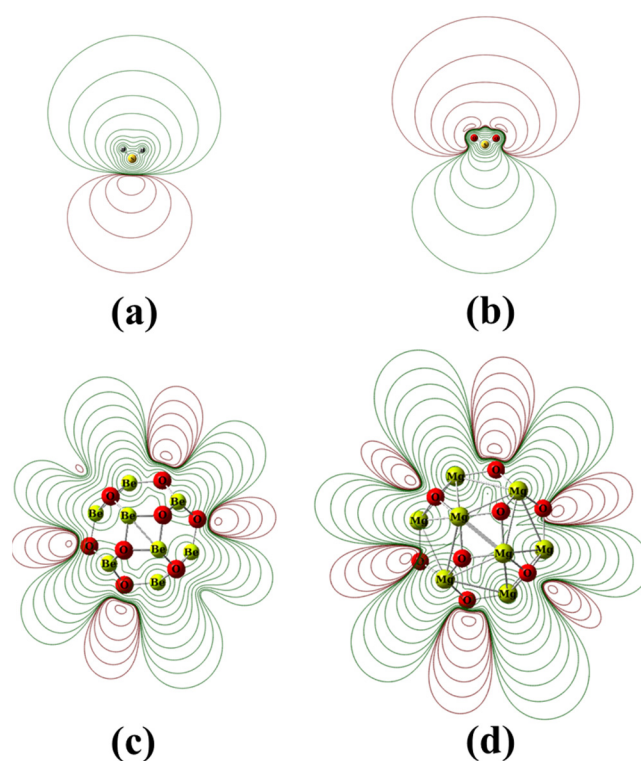
Figure 2. The molecular electrostatic potential contours (MESP) for (**a**) free H_2S gas, (**b**) free SO_2 gas, (**c**) $Be_{12}O_{12,}$ and (**d**) $Mg_{12}O_{12}$ nano-cages at ±0.001, ±0.002, ±0.004,… , ±0.8 au iso-values. Red and green colors are assigned to negative and positive values, respectively.
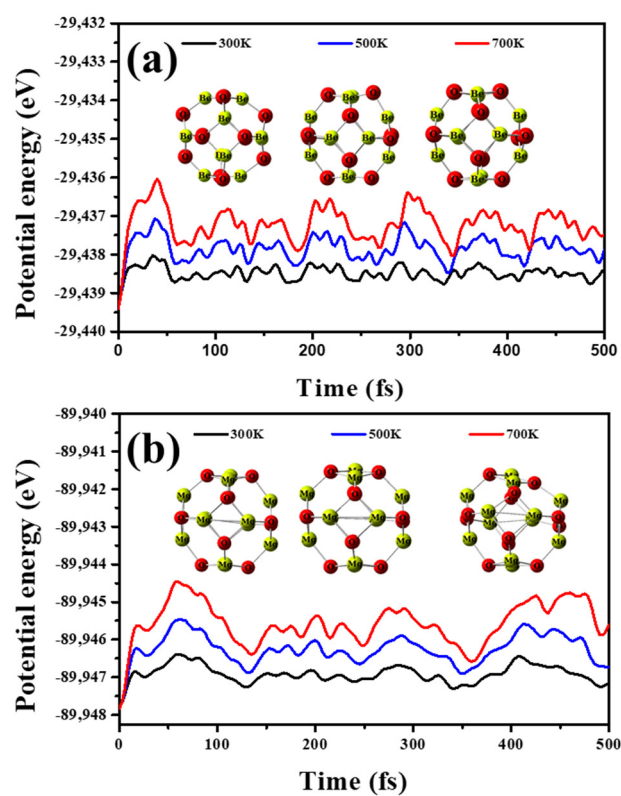

Figure 3. Potential energy fluctuations during MD simulation as well as the atomic configuration after 500 fs at 300, 500, and 700 K for (**a**) $Be_{12}O_{12}$, and (**b**) $Mg_{12}O_{12}$ nano-cages.

It is obvious the potential energy trivially varies and no considerable distortion is observed for the nano-cages; this emphasizes the stability of $Be_{12}O_{12}$ and $Mg_{12}O_{12}$. In addition, the optimized geometries of discussed nano-cages were verified as true minima on the potential energy surfaces by the absence of imaginary frequencies [68–71].

3.2. Adsorption of H_2S and SO_2 Gases

DFT as well DFT-D3 calculations were performed to investigate the adsorption characteristics of the adsorbed gases H_2S and SO_2 at the surfaces of $Be_{12}O_{12}$, as well $Mg_{12}O_{12}$, nano-cages. Four complexes are investigated—$H_2S/Be_{12}O_{12}$, $H_2S/Mg_{12}O_{12}$, $SO_2/Be_{12}O_{12}$, and $SO_2/Mg_{12}O_{12}$. There are several possibilities of the gas interaction with the nano-cage, therefore eight adsorption modes for each complex have been fully optimized without any restrictions. Tables S1 and S2 in the Supplementary Data show the examined adsorption modes for H_2S interaction with $Be_{12}O_{12}$ and $Mg_{12}O_{12}$, respectively. We found that the H_2S prefers to interact via its S atom toward the metallic atom Be or Mg of the nano-cage. Tables S3 and S4 in the Supplementary Data show the examined adsorption modes for SO_2 interaction with $Be_{12}O_{12}$ and $Mg_{12}O_{12}$, respectively. One can observe that SO_2 prefers to interact via its S and O atoms toward the O sites and the metallic atoms, respectively, of the nano-cages. The differences in total electronic energies (ΔE) for the examined orientations are shown in Figure 4.
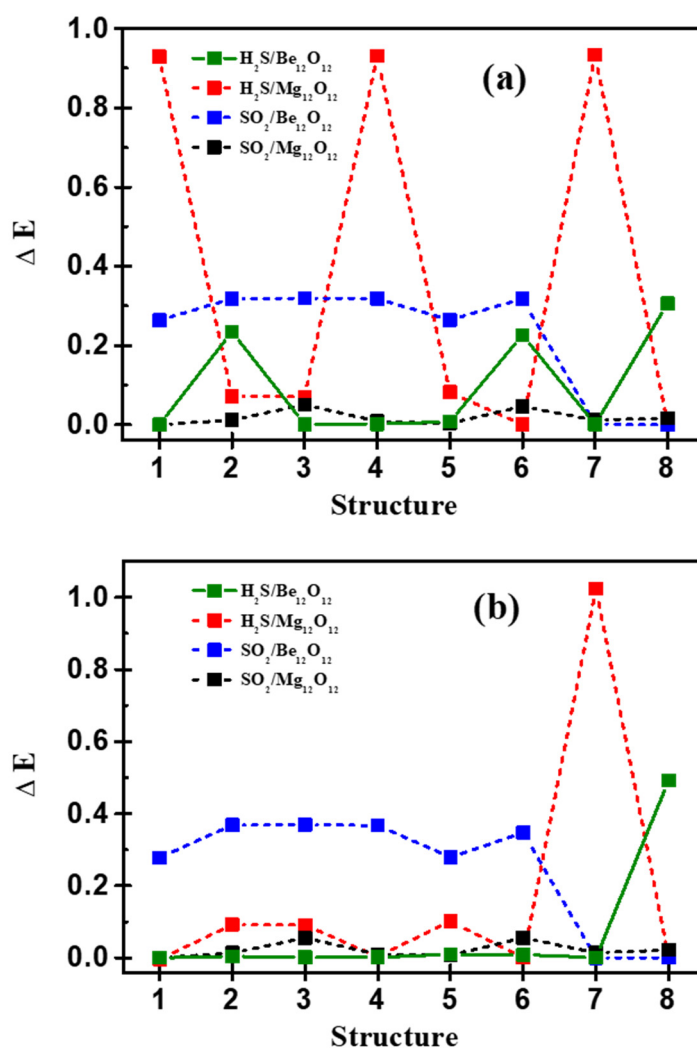

Figure 4. The differences in total electronic energies (ΔE) for the examined structures calculated at (**a**) DFT and (**b**) DFT-D3.

DFT and DFT-D3 calculations show that modes 1, 6, 8, and 1 for $H_2S/Be_{12}O_{12}$, $H_2S/Mg_{12}O_{12}$, $SO_2/Be_{12}O_{12}$, and $SO_2/Mg_{12}O_{12}$, respectively, are the most energetically stable adsorption modes. Figure 5 presents the most energetically stable adsorption modes that have more negative adsorption energy for each complex.

(a)

$d_{25-26} = 1.35$ Å
$d_{25-27} = 1.35$ Å
$d_{1-25} = 2.35$ Å
$A_{26-25-27} = 93.09°$

(b)

$d_{25-26} = 1.35$ Å
$d_{4-26} = 0.98$ Å
$d_{1-25} = 2.40$ Å
$d_{1-4} = 2.99$ Å

(c)

$d_{25-26} = 1.47$ Å
$d_{25-27} = 1.56$ Å
$d_{2-25} = 1.83$ Å
$d_{1-27} = 1.57$ Å
$d_{1-2} = 2.62$ Å
$A_{26-25-27} = 111.35°$

(d)

$d_{25-26} = 1.54$ Å
$d_{25-27} = 1.54$ Å
$d_{2-25} = 1.64$ Å
$d_{7-26} = 2.06$ Å
$d_{3-27} = 1.98$ Å
$d_{2-3} = 2.93$ Å
$A_{26-25-27} = 109.65°$
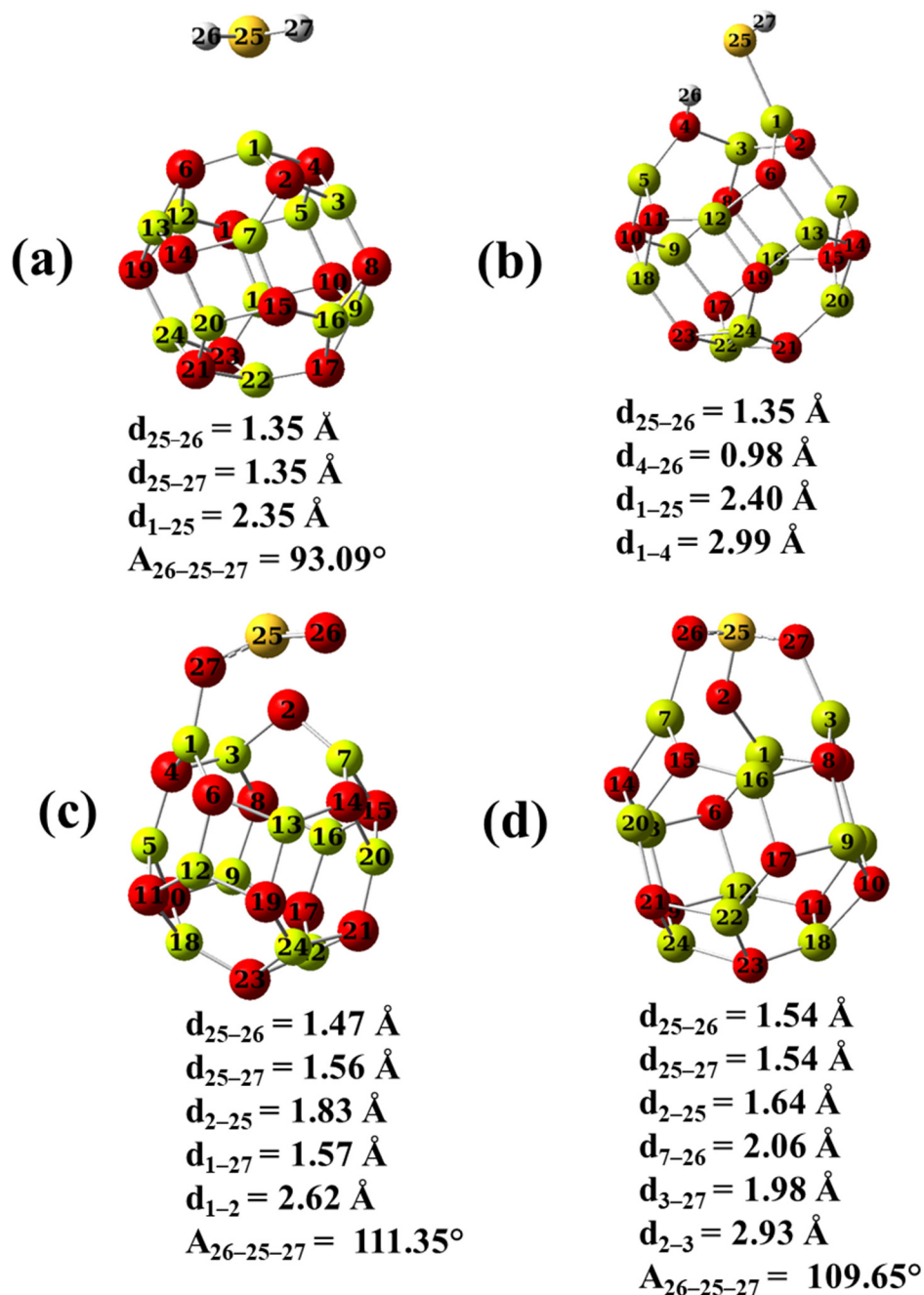
Figure 5. The optimal structures for (**a**) $H_2S/Be_{12}O_{12}$, (**b**) $H_2S/Mg_{12}O_{12}$, (**c**) $SO_2/Be_{12}O_{12}$, and (**d**) $SO_2/Mg_{12}O_{12}$ complexes.

Table 2 list the adsorption properties of H_2S and SO_2. Notably, the DFT-D3 calculations give more negative adsorption energy values than DFT calculations.

Table 2. Adsorption properties of H_2S as well SO_2 on $Be_{12}O_{12}$ and $Mg_{12}O_{12}$ nano-cages. Adsorption energies ($E_{ads.}$, eV), Basis set superposition error (BSSE, eV), corrected adsorption energy (E_{ads}^{corr}, eV), HOMO and LUMO energy levels (eV), HOMO- LUMO gap (E_g, eV), NBO charges (Q, e), and dipole moment (D, Debye).

	H_2S	$H_2S/Be_{12}O_{12}$	$H_2S/Mg_{12}O_{12}$
E_{ads}	-	−0.31 (−0.50)	−1.32 (−1.57)
BSSE	-	0.05 (0.05)	0.09 (0.10)
E_{ads}^{corr}	-	−0.26 (−0.45)	−1.23 (−1.47)
HOMO	−7.31 (−7.31)	−8.20 (−8.22)	−5.93 (−5.95)
LUMO	0.26 (0.26)	−0.67 (−0.68)	−1.94 (−1.93)
E_g	7.56 (7.56)	7.53 (7.54)	3.99 (4.02)
Q_{H_2S}	0.00 (0.00)	0.23 (0.24)	−0.15 (−0.16)
D	1.33 (1.33)	3.27 (3.22)	5.50 (5.48)
	SO_2	$SO_2/Be_{12}O_{12}$	$SO_2/Mg_{12}O_{12}$
E_{ads}	-	−0.83 (−1.07)	−2.33 (−2.52)
BSSE	-	0.38 (0.39)	0.41 (0.41)
E_{ads}^{corr}	-	−0.45 (−0.68)	−1.93 (−2.11)
HOMO	−9.16 (−9.16)	−8.05 (−8.05)	−6.55 (−6.55)
LUMO	−3.73 (−3.73)	−1.47 (−1.49)	−1.84 (−1.83)
E_g	5.43 (5.43)	6.58 (6.57)	4.71 (4.72)
Q_{SO_2}	0.00 (0.00)	−0.13 (−0.13)	−0.34 (−0.34)
D	1.94 (1.94)	2.95 (2.83)	4.59 (4.58)

Values between brackets are calculated at B3LYP/6–311g(d,p) with dispersion correction (DFT-D3).

In contrast, the values for HOMO, LUMO, E_g, Q, and D have no considerable variations between DFT and DFT-D3 calculations. The E_{ads}^{corr} values show that the interaction of H_2S as well SO_2 at the surfaces of $Be_{12}O_{12}$ and $Mg_{12}O_{12}$ is a chemical interaction, where the E_{ads}^{corr} values are lower than −0.2 eV [67]. The released adsorption energy is in the following trend $SO_2/Mg_{12}O_{12}$ > $H_2S/Mg_{12}O_{12}$ > $SO_2/Be_{12}O_{12}$ > $H_2S/Be_{12}O_{12}$. One can notice that the ability of the $Mg_{12}O_{12}$ nano-cage to adsorb the considered gases is higher than that of the $Be_{12}O_{12}$ nano-cage. This is referred to as the higher ability of the $Mg_{12}O_{12}$ nano-cage to donate electrons than the $Be_{12}O_{12}$ nano-cage. Additionally, the ability of the SO_2 gas to be adsorbed on the $Mg_{12}O_{12}$ nano-cage, as well as the $Be_{12}O_{12}$ nano-cage, is higher than that of H_2S gas. Figure 5a shows that the $H_2S/Be_{12}O_{12}$ complex, the S atom of the H_2S molecule, is bonded to a Be site at a distance (d_{1-25}) of 2.35 Å, the S-H bond length is the same as that of the free H_2S molecule, and there is a negligible increase of the H-S-H angle. The H_2S molecule acquires a positive charge of 0.226 e, meaning that a charge transfer has occurred from the H_2S molecule to the $Be_{12}O_{12}$ nano-cage. Figure 5b illustrates the $H_2S/Mg_{12}O_{12}$ complex, while the H_2S molecule dissociates into two fragments HS and H. The HS fragment is bonded via its S atom to a Mg site at a distance (d_{1-25}) of 2.40 Å while the H fragment is attached to an O site at a distance (d_{4-26}) of 0.98 Å. Due to that, an obvious deformation has occurred in $Mg_{12}O_{12}$ where the Mg-O bond length (d_{1-4}) is elongated to 2.99 Å. The net acquired charge by the H_2S molecule is −0.146 e, which means the $Mg_{12}O_{12}$ donates a charge to the H_2S. Figure 5c demonstrates the $SO_2/Be_{12}O_{12}$ complex, while the S atom of the SO_2 molecule is bonded to an O site at a distance (d_{2-25}) of 1.83 Å, and an O atom of the SO_2 molecule is attached to a Be site at a distance (d_{1-27}) of 1.57 Å. While for the SO_2 molecule, the bond length (d_{25-27}) is stretched to 1.56 Å and the O-S-O angle is slightly widened to 111.35°. In addition, the Be-O bond length (d_{1-2}) is elongated to 2.62 Å. The SO_2 molecule gains a negative charge of 0.127 e, i.e., a charge transfer has occurred from the $Be_{12}O_{12}$ nano-cage to the SO_2 molecule. Furthermore, Figure 5d represents the $SO_2/Mg_{12}O_{12}$ complex; it seems that three bonds are formed between the SO_2 molecule and the $Mg_{12}O_{12}$

nano-cage. The two O atoms of the SO_2 molecule are bonded to two Mg sites at distances of (d_{3-27}) 1.98 Å and (d_{7-26}) 2.06Å, while the S atom is attached to an O site at a distance (d_{2-25}) of 1.64 Å. In addition, the two S-O bonds of the SO_2 molecule are dilated to 1.54 Å while the O-S-O angle is diminished to 109.6° and the Mg-O bond length (d_{2-3}) is elongated to 2.93 Å. Moreover, the SO_2 molecule accepts a negative charge of −0.339 e; therefore, a charge transfer has occurred from the $Mg_{12}O_{12}$ nano-cage to the SO_2 molecule. Additionally, the adsorption of H_2S leads to a decrease in the HOMO–LUMO gap (E_g) values of $Be_{12}O_{12}$ and $Mg_{12}O_{12}$ by 3.84% and 17.54%, respectively, whereas the adsorption of SO_2 leads to a decrease in E_g values by 15.97% and 2.60%, respectively. Therefore, one can say that the E_g of the $Be_{12}O_{12}$ nano-cage is more sensitive to the SO_2 than H_2S adsorption while the E_g of the $Mg_{12}O_{12}$ nano-cage reveals higher sensitivity to H_2S than SO_2 adsorption.

The electrical conductivity (σ) and recovery time (τ) are important aspects of sensing applications. σ depends on E_g according to the following equation [72–77]:

$$\Delta G = G_{gas/nano-cage} - (G_{gas} + G_{nano-cage}) \tag{10}$$

where A is a constant, k is Boltzmann's constant, and T is the temperature. Therefore, the increase of σ value of the $Be_{12}O_{12}$ nano-cage in the presence of SO_2 gas is higher than in the presence of H_2S gas, while the increase of σ value of the $Mg_{12}O_{12}$ nano-cage in the presence of H_2S gas is higher than in the presence of SO_2 gas. The τ is related to the E_{ads} as in Equation (11) [78,79]:

$$\tau = v_0^{-1} \exp(\frac{-E_{ads}}{KT}) \tag{11}$$

where v_0 is the attempt frequency. In other words, as E_{ads} increases (more negative) the longer τ becomes. Therefore, in the obtained E_{ads} values, τ trends as follows: $SO_2/Mg_{12}O_{12}$ > $H_2S/Mg_{12}O_{12}$ > $SO_2/Be_{12}O_{12}$ > $H_2S/Be_{12}O_{12}$. Thus, our results may be fruitful for sensing applications.

To illuminate the features of the interaction between the considered gases and the sorbent nano-cages, our results will be discussed related to the following: (i) NBO atomic charges as well charge density difference analysis ($\Delta\rho$), (ii) bond analysis, and (iii) PDOS analysis.

3.2.1. NBO and Charge Density Difference Analysis

To shed light on the mechanism of H_2S and SO_2 interaction with the considered nano-cages, NBO analysis, as well as charge density difference ($\Delta\rho$) analysis, has been performed. Table 3 lists the atomic NBO charges, as well the electronic configuration of the atoms, for the free H_2S, $Be_{12}O_{12}$, $Mg_{12}O_{12}$, $H_2S/Be_{12}O_{12}$, and $H_2S/Mg_{12}O_{12}$. The numbering of atoms as shown in Figure 5 is used.

Table 3. NBO charges (Q, e) and electronic configuration for free H_2S, $Be_{12}O_{12}$, $Mg_{12}O_{12}$, $H_2S/Be_{12}O_{12}$, and $H_2S/Mg_{12}O_{12}$.

Structure	Atom	Atomic Charge	Electronic Configuration				
			1s	2s	2p	3s	3p
H_2S	H	0.134	0.86	-	-	-	-
	S	−0.268	-	-	-	1.76	4.48
$Be_{12}O_{12}$	Be	1.186	-	0.21	0.59	-	-
	O	−1.186	-	1.69	5.49	-	-
$Mg_{12}O_{12}$	Mg	1.443	-	-	-	0.21	0.35
	O	−1.443	-	1.84	5.60	-	-
$H_2S/Be_{12}O_{12}$	H26	0.160	0.83	-	-	-	-
	H27	0.159	0.84	-	-	-	-
	S	−0.093	-	-	-	1.73	4.34
	Be1	1.007	-	0.25	0.73	-	-

	O2	−1.191	-	1.68	5.50	-	-
	O4	−1.189	-	1.68	5.50	-	-
	O6	−1.190	-	1.68	5.50	-	-
$H_2S/Mg_{12}O_{12}$	H26	0.509	0.49	-	-	-	-
	H27	0.130	0.86	-	-	-	-
	S	−0.785	-	-	-	1.81	4.97
	Mg1	1.305	-	-	-	0.27	0.41
	O2	−1.452	-	1.83	5.62	-	-
	O4	−1.251	-	1.77	5.47	-	-
	O6	−1.442	-	1.83	5.61	-	-

For the $H_2S/Be_{12}O_{12}$ structure, it is clear that due to the interaction, the 1s orbital of the H26 and H27 atoms loses charges of 0.03 and 0.02 e while the 3s and 3p orbitals of the S atom lose charges of 0.03 and 0.14 e, respectively. On the other hand, the 2s and 2p orbitals of the Be1 atom gain charges of 0.14 and 0.04 e while for the O2, O4, and O6 the 2s orbital loses a charge of 0.01e whereas the 2p orbital gains a charge of 0.01 e. This explains why a total charge of 0.226 e, as shown in Table 2, has been transferred from H_2S to the $Be_{12}O_{12}$ nano-cage and the major of the charge transfer has occurred from the S atom of H_2S to the Be1 atom of the $Be_{12}O_{12}$ nano-cage.

This means the major mechanism of the interaction is the charge transfer mechanism. In addition, a slight loss and gain of charges are observed simultaneously for the O2, O4, and O6; therefore, one can suggest another minor mechanism which is the donation–back donation mechanism. Figure 6a demonstrates $\Delta\rho$ for $H_2S/Be_{12}O_{12}$ complex.
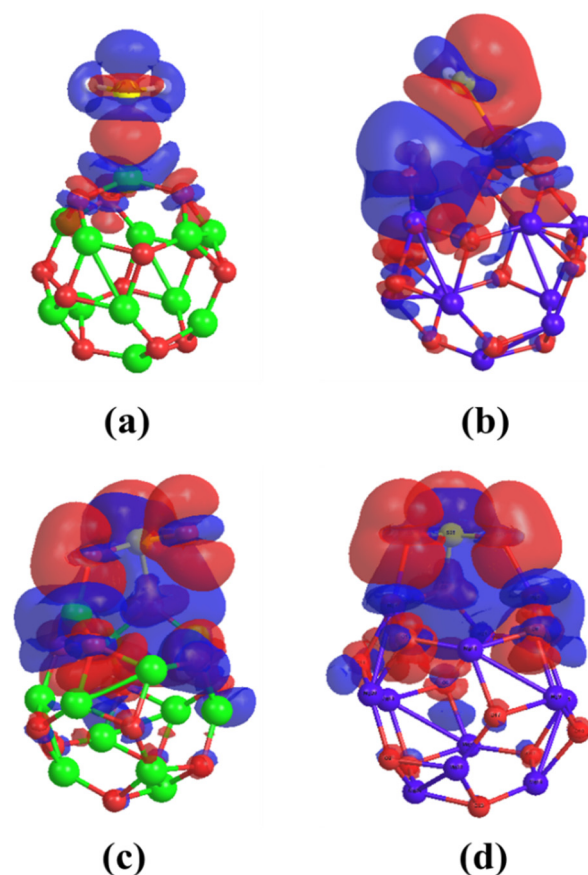

(a)　　　　　　　　**(b)**

(c)　　　　　　　　**(d)**

Figure 6. Charge density difference ($\Delta\rho$) for (**a**) $H_2S/Be_{12}O_{12}$, (**b**) $H_2S/Mg_{12}O_{12}$, (**c**) $SO_2/Be_{12}O_{12}$, and (**d**) $SO_2/Mg_{12}O_{12}$ complexes. Red color for negative $\Delta\rho$ and blue color for positive $\Delta\rho$.

The H and S atoms of the H_2S molecule are surrounded by positive $\Delta\rho$ values (blue color), which confirms the charge transfer from the H_2S molecule to the nano-cage. In addition, the positive (blue color) and negative (red color) $\Delta\rho$ values around each of the O2, O4, O6, and S atoms confirm the donation–back donation mechanism. For $H_2S/Mg_{12}O_{12}$ structure, the interaction between H_2S and $Mg_{12}O_{12}$ leads to the following: the 1s orbital of the H26 loses a charge of 0.37 e whereas the 2s and 2p of the O4 atom lose a charge of 0.07 and 0.13 e, respectively. Furthermore, the H27 atom has no change, the 3s and 3p orbitals of the S atom gain charges of 0.05 and 0.49 e, and the 3s and 3p of the Mg gain charges of 0.06 and 0.06 e, respectively. This confirms the dissociation of the H_2S molecule into H^+ and SH^-. Then, the H^+ is attached to the O4 atom, while the SH^- is attached to the Mg1 atom. Figure 6b shows $\Delta\rho$ for the $H_2S/Mg_{12}O_{12}$ complex. The H26 is surrounded by positive $\Delta\rho$ values (blue color) while the S atom is surrounded by negative (red color) $\Delta\rho$ values which agree with the above discussion. Table 4 illustrates the atomic NBO charges, as well the electronic configuration of the atoms, for the free SO_2, $Be_{12}O_{12}$, $Mg_{12}O_{12}$, $SO_2/Be_{12}O_{12}$, and $SO_2/Mg_{12}O_{12}$.

Table 4. NBO charges (Q, e) and electronic configuration for free SO_2, $Be_{12}O_{12}$, $Mg_{12}O_{12}$, $SO_2/Be_{12}O_{12}$, and $SO_2/Mg_{12}O_{12}$.

Structure	Atom	Atomic Charge	Electronic Configuration			
			2s	2p	3s	3p
SO_2	O	−0.747	1.84	4.89	-	-
	S	1.495	-	-	1.62	2.68
$Be_{12}O_{12}$	Be	1.186	0.21	0.59	-	-
	O	−1.186	1.69	5.49	-	-
$Mg_{12}O_{12}$	Mg	1.443	-	-	0.21	0.35
	O	−1.443	1.84	5.60	-	-
$SO_2/Be_{12}O_{12}$	O26	−0.852	1.84	5.00	-	-
	O27	−0.980	1.76	5.21	-	-
	S	1.705	-	-	1.55	2.58
	Be1	1.210	0.22	0.55	-	-
	O2	−1.109	1.75	5.36	-	-
	O4	−1.214	1.69	5.52	-	-
	O6	−1.197	1.69	5.50	-	-
$SO_2/Mg_{12}O_{12}$	O26	−1.003	1.82	5.17	-	-
	O27	−1.049	1.81	5.23	-	-
	S	1.713	-	-	1.51	2.62
	Mg1	1.477	-	-	0.20	0.32
	Mg3	1.468	-	-	0.20	0.32
	Mg7	1.417	-	-	0.21	0.36
	O2	−1.148	1.82	5.32	-	-
	O4	−1.463	1.84	5.62	-	-
	O8	−1.454	1.84	5.61	-	-

For $SO_2/Be_{12}O_{12}$ structure, one can observe, that the 2s of the O27 and the 3s and 3p of the S atom lose charges of 0.08, 0.07, and 0.10 e, respectively, while the 2p of the O26 and O27 atoms gain charges of 0.11 and 0.32 e, respectively. Therefore, the positive charge of the S atom and the negative charge of the O27 atom increase; consequently, they are attached to the O2 negative and Mg1 positive sites of the nano-cage, respectively. Moreover, for the Be1 atom, the 2s gains a charge of 0.01 e while the 2p loses a charge of 0.04 e, whereas for the O2 atom, the 2s gains a charge of 0.06 e while the 2p orbital loses a charge of 0.13 e. Therefore, one can say that there is a charge transfer from the $Be_{12}O_{12}$ nano-cage to the SO_2 molecule greater than the charge transferred from the SO_2 molecule to the

$Be_{12}O_{12}$ nano-cage. This explains why SO_2 has a total charge of −0.127 e, as shown in Table 2. $\Delta\rho$ for the $SO_2/Be_{12}O_{12}$ complex is demonstrated in Figure 6c. It is clear that both the adsorbed SO_2 molecule and the sorbent $Be_{12}O_{12}$ nano-cage are surrounded by positive and negative $\Delta\rho$ values (blue and red colors) which confirms the donation–back donation mechanism for the interaction. For the $SO_2/Mg_{12}O_{12}$ structure, one can notice that the 2s of the O26 and O27 loses charges of 0.02 and 0.03 e while the 2p gains charges of 0.28 and 0.34 e, respectively. Moreover, the 3s and 3p of the S atom lose charges of 0.11 and 0.06 e, respectively. Therefore, the net atomic charges of the O atoms of the SO_2 become more negative while the S atom becomes more positive, consequently, the O26 and O27 are attracted to the Mg7 and Mg3 positive sites while the S atom is attracted to the O2 negative site of the $Mg_{12}O_{12}$ nano-cage, whereas for the $Mg_{12}O_{12}$, the 2s and 2p of the O2 atom lose charges of 0.02 and 0.28 e while the rest atoms of the nano-cage have little gains and loss of charges. $\Delta\rho$ for the $SO_2/Mg_{12}O_{12}$ complex is illustrated in Figure 6d. It is clear that the adsorbed SO_2 molecule is surrounded by negative $\Delta\rho$ values greater than the positive $\Delta\rho$ values, which confirm the donation–back donation mechanism for the interaction.

3.2.2. Bond Analysis

Bond order and overlap population are estimated for the free adsorbed gasses as well gas/nano-cage complexes. As the overlap value decreases, the interaction between the two atoms decreases and vice versa whereas the values close to zero mean no interaction while overlapping positive and negative values indicate the bonding and anti-bonding states, respectively [71,75,80]. Table 5 concerns the free H_2S molecule, $H_2S/Be_{12}O_{12}$, and $H_2S/Mg_{12}O_{12}$ complexes.

Table 5. Overlap population and bond order of H_2S, $H_2S/Be_{12}O_{12}$, and $H_2S/Mg_{12}O_{12}$.

Structure	H_2S		$H_2S/Be_{12}O_{12}$		$H_2S/Mg_{12}O_{12}$	
	Overlap Pop.	Bond Order	Overlap Pop.	Bond Order	Overlap Pop.	Bond Order
S–H26	0.304	0.979	0.316	0.974	0.042	0.097
S–H27	0.304	0.979	0.313	0.972	0.266	0.956
S–M1	-	-	0.074	0.279	0.273	0.717
O4–H26	-	-	0.000	0.002	0.289	0.835
M1–O4	-	-	0.206 (0.220) *	0.538 (0.602) *	0.035 (0.183) *	0.106 (0.520) *

* Values between brackets are for the bare nano-cage. M = Be and Mg.

For $H_2S/Be_{12}O_{12,}$ the overlap population and bond order values of the S-H26 and S-H27 bonds are slightly changed with respect to the free H_2S molecule, while overlapping population and bond order values of 0.074 and 0.279, respectively, are observed for the S-Be1 bond. This indicates the formation of a weak bond between the H_2S molecule and the $B_{12}O_{12}$ nano-cage. On the other hand, for $H_2S/Mg_{12}O_{12}$, the low overlap population and bond order values for the S-H26 bond indicate the dissociation of the H_2S molecule. In addition, high overlapping population and bond order values for S-Mg1 and O4-H26 indicate bond formation between the S atom and the Mg1 atom and between the H26 atom and the O4 atom. Furthermore, the overlapping population and the bond order values for the Mg1-O4 are decreased to 0.035 and 0.106 rather than 0.183 and 0.520 for the bare nano-cage, respectively, indicating a bond weakness has occurred. This reveals the strong interaction between the H_2S molecule and the $Mg_{12}O_{12}$ nano-cage. Table 6 is interested in the free SO_2 molecule, $SO_2/Be_{12}O_{12}$, and $SO_2/Mg_{12}O_{12}$ complexes.

For $SO_2/Be_{12}O_{12}$, the S-O27 and Be1-O2 bonds are weakened as indicated by the low values of the overlap population and bond order, while the high overlap population and bond order values for the Be1-O27 bond indicate bond formation. On the other hand, for $SO_2/Mg_{12}O_{12}$, the decrease in the S-O26, S-O27, and Mg3-O2 overlapping population and bond order values indicates the weakness of these bonds while the bond order of 0.892, 0.464, and 0.495 for the S-O2, Mg-O27, and Mg-O26, respectively, confirms the formation

of these bonds. In other words, one bond is formed between the SO_2 and the nano-cage for the $SO_2/Be_{12}O_{12}$ complex, whereas three bonds are formed for the $SO_2/Mg_{12}O_{12}$ complex. This explains the higher adsorption energy for $SO_2/Mg_{12}O_{12}$ than $SO_2/Be_{12}O_{12}$.

Table 6. Overlap population and bond order of SO_2, $SO_2/Be_{12}O_{12}$, and $SO_2/Mg_{12}O_{12}$.

Structure	SO$_2$		SO$_2$/Be$_{12}$O$_{12}$		SO$_2$/Mg$_{12}$O$_{12}$	
	Overlap Pop.	Bond Order	Overlap Pop.	Bond Order	Overlap Pop.	Bond Order
S-O26	0.242	1.773	0.302	1.706	0.203	1.290
S-O27	0.242	1.773	0.116	1.138	0.156	1.219
S-O2	-	-	−0.015	0.564	0.079	0.892
M1-O27	-	-	0.262	0.614	0.000	−0.010
M3-O27	-	-	0.022	0.022	0.192	0.464
M7-O26	-	-	0.057	0.118	0.207	0.495
M1-O2	-	-	−0.006 (0.220)*	0.028 (0.602)*	0.113 (0.183)*	0.267 (0.520)*
M3-O2	-	-	0.215 (0.220)*	0.452 (0.602)*	0.033 (0.183)*	0.103 (0.520)*

* Values between brackets are for the bare nano-cage. M = Be and Mg.

3.2.3. PDOS Analysis

Figure 7 illustrates the surfaces of the HOMO and LUMO as well as the PDOS for the free H_2S molecule, the bare $Be_{12}O_{12}$, and $Mg_{12}O_{12}$ nano-cages, as well the $H_2S/Be_{12}O_{12}$ and $H_2S/Mg_{12}O_{12}$ complexes.

Figure 7a shows three occupied states for the H_2S molecule at −12.36, −10.12, and −7.30 eV; the H atom states located at −12.36 and −10.12 eV; and the S atom states located at −12.36, −10.12, and −7.35 eV. The S atom states for free H_2S molecule are disappeared in the $H_2S/Be_{12}O_{12}$ complex, as shown in Figure 7c. Furthermore, new states for the S atom are observed in the $H_2S/Be_{12}O_{12}$ complex; these states overlap with the Be and O states, which emphasizes the interaction between the H_2S molecule with the nano-cage. For instance, the states of the S, Be, and O atoms of the complex are overlapped at −8.20 eV, which is the HOMO of the complex. The HOMO surface of the complex displays the contribution of the S, Be, and O atoms. Comparing Figure 7b,c, one can observe the adsorption of the H_2S molecule rises the HOMO and LUMO of $Be_{12}O_{12}$ by 0.43 and 0.13 eV, respectively; therefore, a decrease of 0.30 eV in the HOMO–LUMO gap has been recorded. For $H_2S/Mg_{12}O_{12}$ complex, Figure 7e, it is clear that there is an overlap between the H and O states at −12.92 eV, which is due to the interaction between H26 and O4 in the complex. Moreover, the occupied states of the S atom are located at −9.70, −6.51, and −5.93 eV, i.e., they are shifted up with respect to the free H_2S, which confirms the strong interaction between the H_2S and $Mg_{12}O_{12}$ nano-cage. In addition, comparing Figure 7d,e, one can see that HOMO rises by 1.02 eV while LUMO lowers by 0.19 eV. Thus, H_2S adsorption narrows the HOMO–LUMO gap by 0.85 eV. It is worth noticing that only the states of S and O atoms appear in the HOMO states, and this agrees with the obtained HOMO surface for the $H_2S/Mg_{12}O_{12}$ complex. Figure 8 demonstrates the surfaces of HOMO and LUMO, as well PDOS, for the free SO_2 molecule, bare $Be_{12}O_{12}$, and $Mg_{12}O_{12}$ nano-cages, as well $SO_2/Be_{12}O_{12}$ and $SO_2/Mg_{12}O_{12}$ complexes.
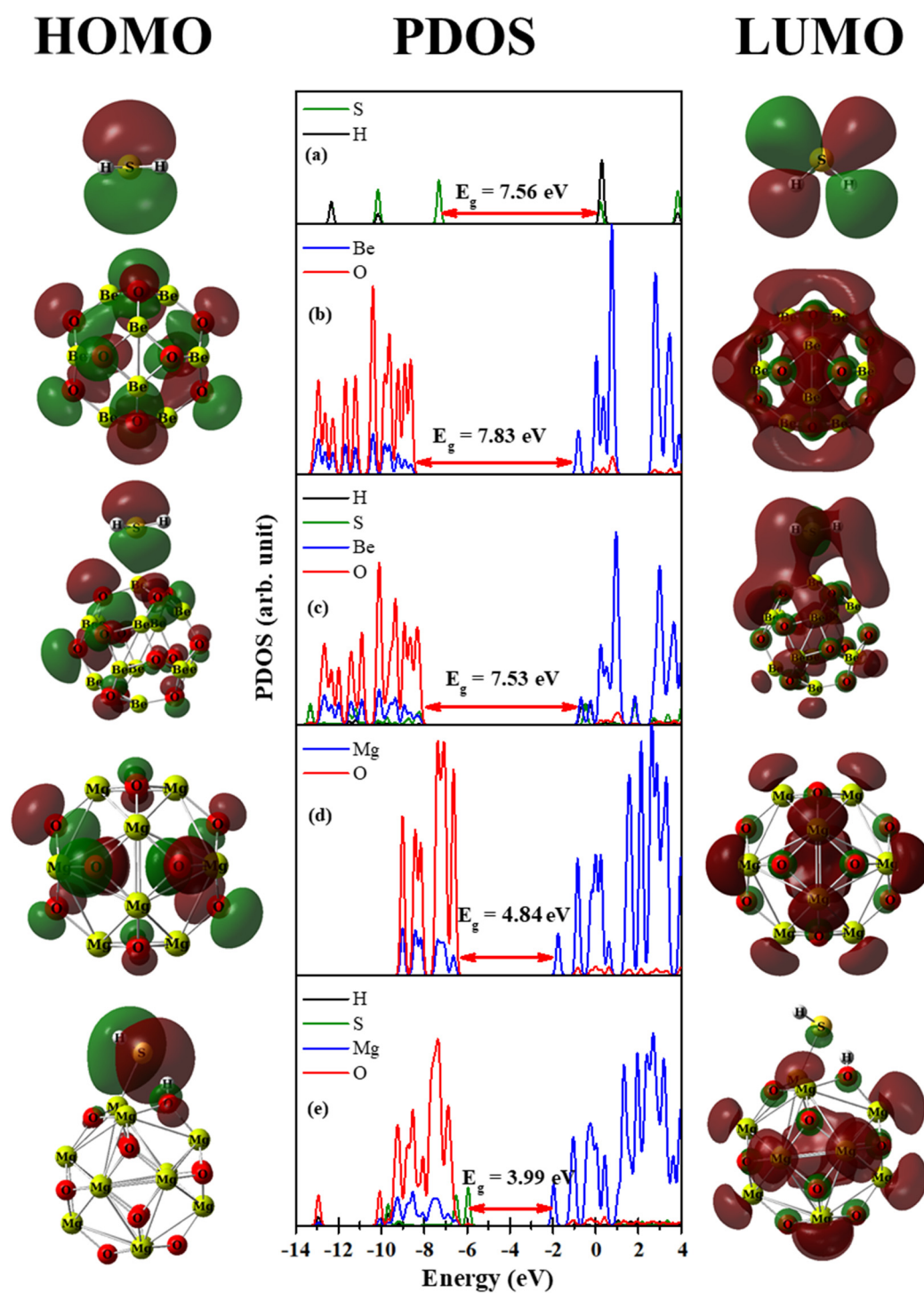
Figure 7. HOMO, PDOS, LUMO for (**a**) H_2S, (**b**) $Be_{12}O_{12}$, (**c**) $H_2S/Be_{12}O_{12}$, (**d**) $Mg_{12}O_{12}$, and (**e**) $H_2S/Mg_{12}O_{12}$ complexes.
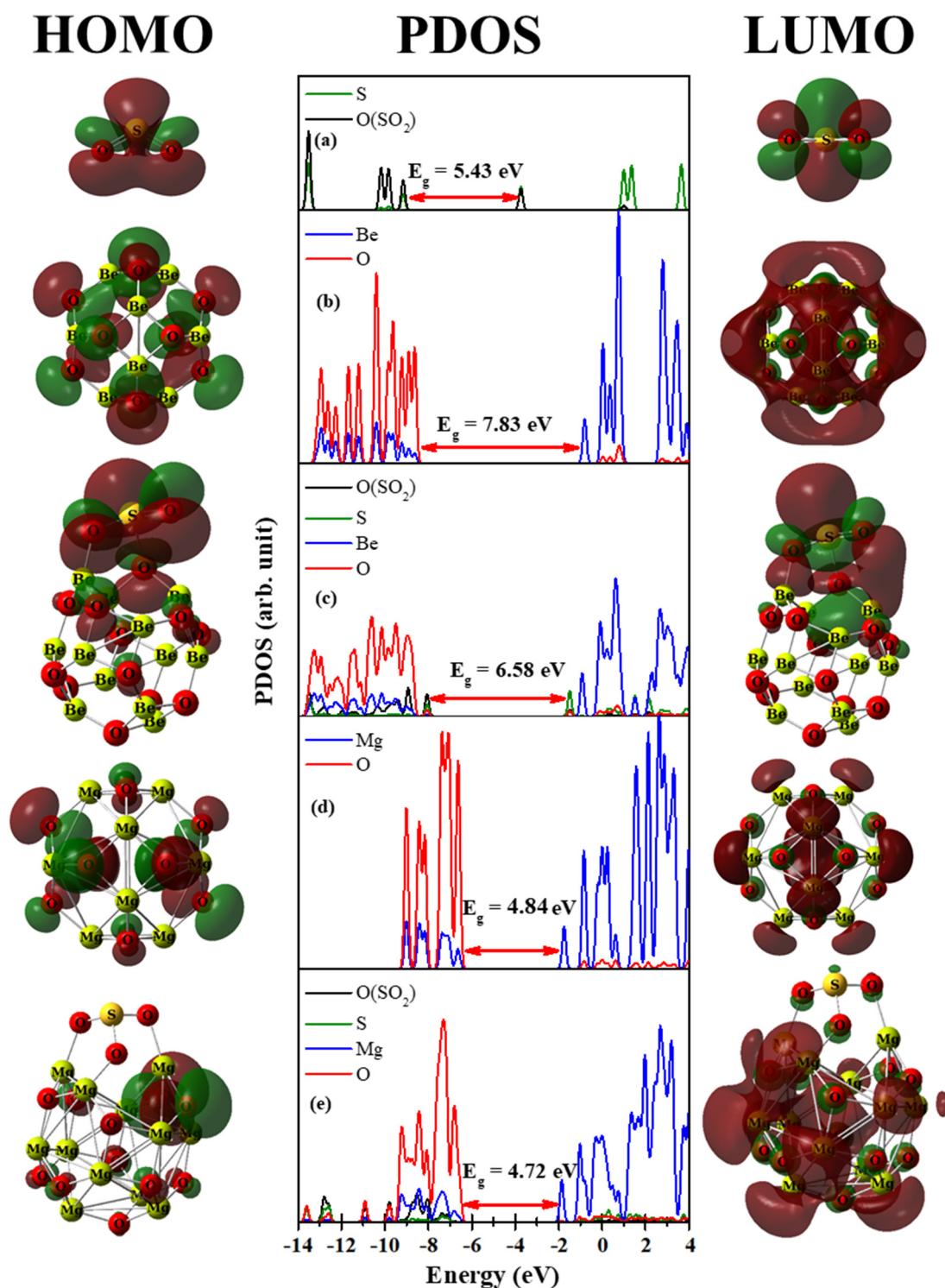
Figure 8. HOMO, PDOS, LUMO for (**a**) SO_2, (**b**) $Be_{12}O_{12}$, (**c**) $SO_2/Be_{12}O_{12}$, (**d**) $Mg_{12}O_{12}$, and (**e**) $SO_2/Mg_{12}O_{12}$ complexes.

Comparing Figure 8a–c, it is clear that there are dramatic changes in the states due to the adsorption of the SO_2 molecule on the $Be_{12}O_{12}$ nano-cage, where the states of SO_2 overlap with the states of $Be_{12}O_{12}$. For example, one can observe the appearance of the S atom and the O atoms of the SO_2 and $Be_{12}O_{12}$ in the HOMO states of the $SO_2/Be_{12}O_{12}$ at −8.05 eV. This is confirmed by the HOMO surface for the $SO_2/Be_{12}O_{12}$ complex. Based on the interaction, the HOMO of the nano-cage rises by 0.57 eV and the LUMO lowers by 0.68 eV, in

turn, narrowing the HOMO–LUMO gap by 1.25 eV. Comparing Figure 8a,d,e, one can observe that adsorption of the SO_2 molecule on the $Mg_{12}O_{12}$ nano-cage leads to intense changes in the states of the SO_2 as well as the states of the $Mg_{12}O_{12}$, which confirms the occurrence of a strong interaction. Moreover, the HOMO of the nano-cage increases by 0.04 while the LUMO decreases by 0.08 eV; consequently, the HOMO–LUMO gap is slightly decreased by 0.12 eV.

3.3. Molecular Dynamic Simulations

To examine the impact of the temperature on the adsorption process of the investigated gases, molecular dynamic (MD) simulations at 300, 500, and 700 K for a total time of 500 fs are performed for $H_2S/Be_{12}O_{12}$, $H_2S/Mg_{12}O_{12}$, $SO_2/Be_{12}O_{12}$, and $SO_2/Mg_{12}O_{12}$ complexes. MD simulations are carried out via the ADMP model. Figure 9a,b illustrates the potential energy fluctuations for $H_2S/Be_{12}O_{12}$ and $H_2S/Mg_{12}O_{12}$, respectively, as well as the atomic configuration after 500 fs at the inspected temperatures.
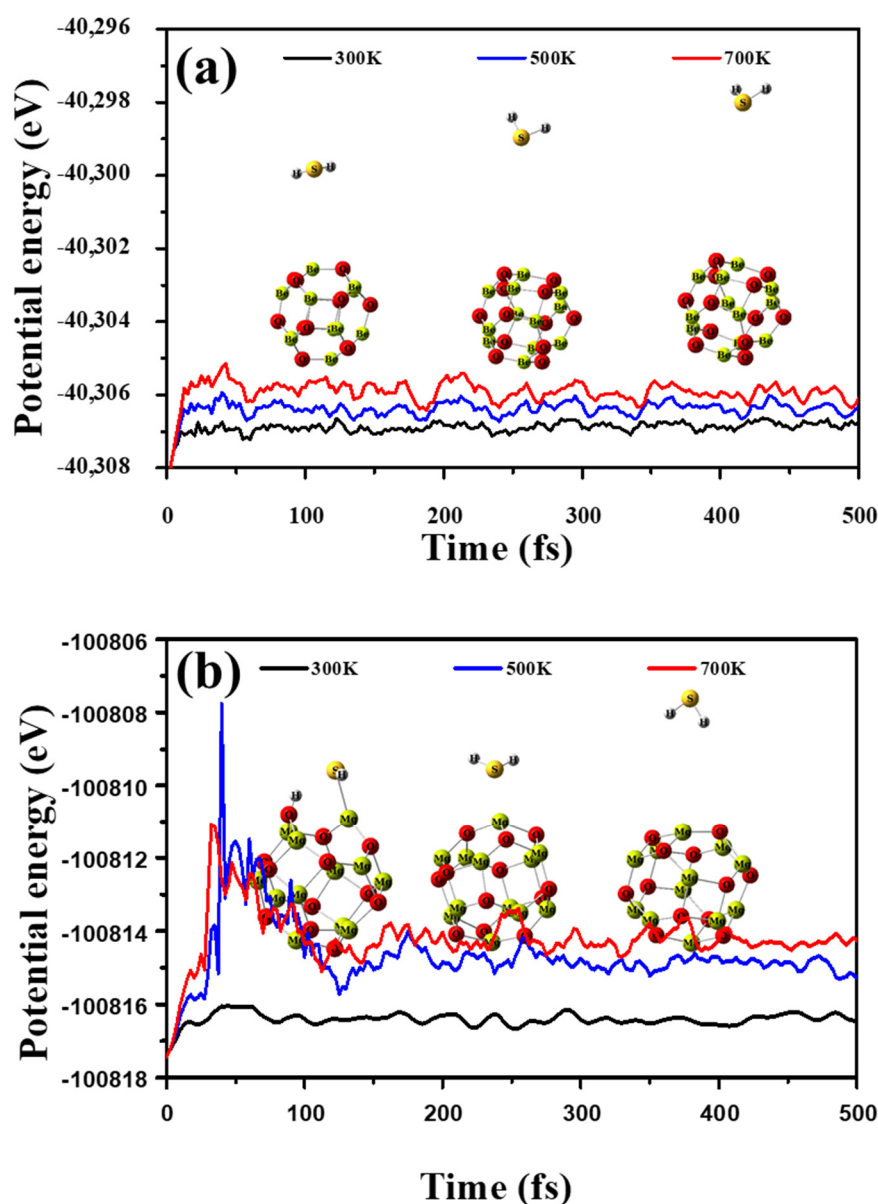
Figure 9. Potential energy fluctuations during MD simulation for (**a**) $H_2S/Be_{12}O_{12}$, and (**b**) $H_2S/Mg_{12}O_{12}$ and the atomic configuration after 500 fs at 300, 500, and 700 K.

For $H_2S/Be_{12}O_{12}$ Figure 9a, although the fluctuation of the potential energy is small, the distance (d_{1-25}) between H_2S and $Be_{12}O_{12}$ nano-cage increased with time. As well as the temperature increases, the increment in the distance increases, where the d_{1-25} values at the end of the time increase to 3.32, 7.38, and 9.55 Å for temperatures 300, 500, and 700 K, respectively. Therefore, one suggests that the $Be_{12}O_{12}$ nano-cage cannot retain H_2S on its surface, especially at high temperatures. For $H_2S/Mg_{12}O_{12}$, Figure 9b, at the temperature of 300 K, the fluctuation of the potential energy is small, and the $Mg_{12}O_{12}$ nano-cage preserves the dissociated H_2S molecule on its surface with no significant changes in the geometrical structure of the complex, while at the temperatures of 500 and 700 K, a high fluctuation of the potential energy is observed until 120–130 fs, when the fluctuation decreases. In addition, the dissociation of the H_2S molecule is diminished. At the end of the time, at 500 K, the H_2S is retained on the $Mg_{12}O_{12}$ nano-cage at a distance of 2.65 Å while at 700 K the d_{1-25} increases to 6.79 Å. Furthermore, Figure 10a,b demonstrates the potential energy fluctuations for $SO_2/Be_{12}O_{12}$ and $SO_2/Mg_{12}O_{12}$, respectively, as well as the atomic configuration after 500 fs at the inspected temperatures.

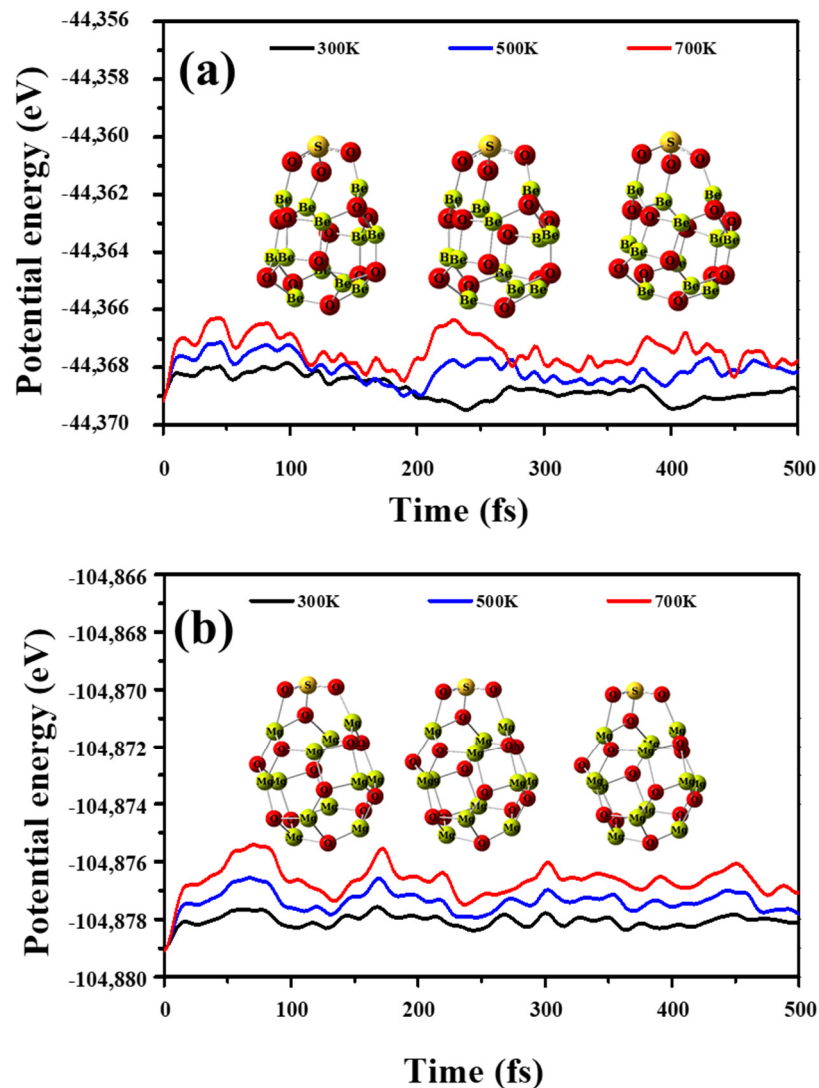**Figure 10.** Potential energy fluctuations during MD simulation for (**a**) $SO_2/Be_{12}O_{12}$, and (**b**) $SO_2/Mg_{12}O_{12}$ and the atomic configuration after 500 fs at 300, 500, and 700 K.

It is clear that no significant fluctuation of the potential energy is observed. Moreover, at the end of the time, there is a trivial deformation in the geometrical structure of the

SO$_2$/Be$_{12}$O$_{12}$ and SO$_2$/Mg$_{12}$O$_{12}$ complexes. Therefore, one proposes that Be$_{12}$O$_{12}$ and Mg$_{12}$O$_{12}$ nano-cages can retain the SO$_2$ molecule on their surface at temperatures up to 700 K.

3.4. Thermodynamic Properties

For gas adsorption, enthalpy difference (ΔH) and free energy difference (ΔG) are imperative thermodynamic parameters for determining the strength and the spontaneity of the reaction. Therefore, thermodynamic calculations for H$_2$S/Be$_{12}$O$_{12}$, H$_2$S/Mg$_{12}$O$_{12}$, SO$_2$/Be$_{12}$O$_{12}$, and SO$_2$/Mg$_{12}$O$_{12}$ complexes have been performed in the temperature range 300–700 K. Figure 11a signifies ΔH for the investigated complexes.
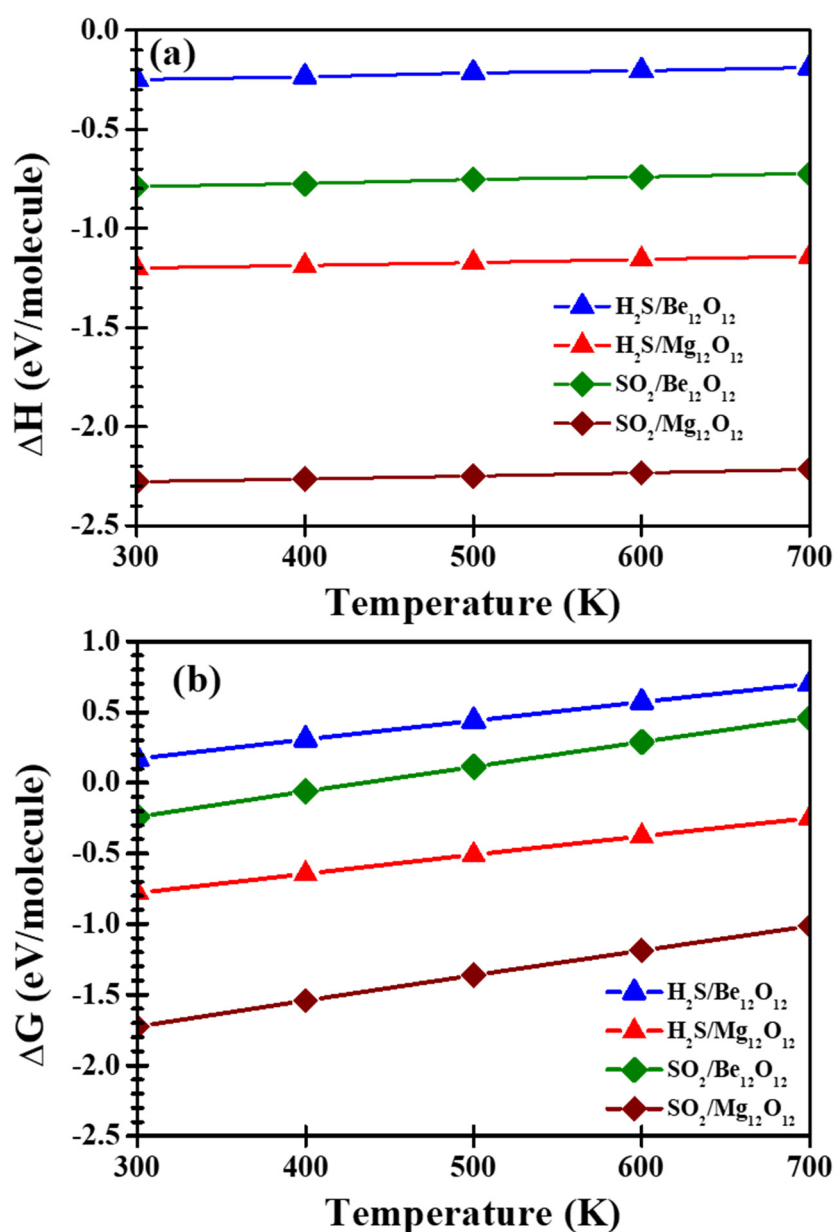

Figure 11. (**a**) ΔH and (**b**) ΔG for H$_2$S/Be$_{12}$O$_{12}$, H$_2$S/Mg$_{12}$O$_{12}$, SO$_2$/Be$_{12}$O$_{12}$, and SO$_2$/Mg$_{12}$O$_{12}$ complexes.

ΔH values for all considered complexes are negative, which specifies the reactions between H$_2$S as well SO$_2$ with Be$_{12}$O$_{12}$ and Mg$_{12}$O$_{12}$ nano-cages are exothermic. Furthermore, as the temperature increases, the negative ΔH values decrease, which indicates the

reactions are stronger at lower temperatures. In addition, for the same gas, ΔH values are more negative for the $Mg_{12}O_{12}$ nano-cage than the $Be_{12}O_{12}$ nano-cage, while for the same nano-cage, ΔH values are more negative for SO_2 gas than H_2S gas. This confirms the above discussion of the high ability of the $Mg_{12}O_{12}$ nano-cage to absorb the investigated gases and the high ability of the SO_2 gas to attach to the considered nano-cages. Figure 11b shows ΔG for the examined complexes. Spontaneous and non-spontaneous reactions are characterized by negative and positive ΔG values, respectively, while low negative ΔG values indicate the capability to reverse the reaction [46,66–68]. For the $H_2S/Be_{12}O_{12}$ complex in the temperature range, ΔG values are positive, which indicates a non-spontaneous reaction, while for the $SO_2/Be_{12}O_{12}$ complex, the reaction is spontaneous at low temperatures, and beyond T = 400 K, the reaction turns into a non-spontaneous reaction. Furthermore, for the $H_2S/Mg_{12}O_{12}$ and $SO_2/Mg_{12}O_{12}$ complexes in the temperature range, ΔG values are negative, which indicates a spontaneous reaction. In addition, the reaction is capable of being reversed in the $H_2S/Mg_{12}O_{12}$ complex easier than in the $SO_2/Mg_{12}O_{12}$ complex.

4. Conclusions

Structural and electronic properties of the considered $Be_{12}O_{12}$ and $Mg_{12}O_{12}$ nano-cages as well their stability are scrutinized. $Mg_{12}O_{12}$ exhibits lower E_g, IP, η, and higher ω values than those for $Be_{12}O_{12}$; therefore, $Mg_{12}O_{12}$ is more reactive than the $Be_{12}O_{12}$ nano-cage. Molecular dynamics calculations emphasize the stability of the investigated nano-cages. In addition, the interaction of H_2S and SO_2 gases at the surfaces of the inspected nano-cages have been studied, and the features of the interaction are examined in the point of the NBO atomic charges, charge density difference analysis (Δρ), bond analysis, and PDOS. E_{ads}^{corr} values show that the ability of the $Mg_{12}O_{12}$ nano-cage to adsorb the considered gases is higher than that of the $Be_{12}O_{12}$ nano-cage. Furthermore, the ability of SO_2 gas to be adsorbed is higher than that of H_2S gas. Furthermore, H_2S gas dissociates at the $Mg_{12}O_{12}$ surface. In addition, adsorption of H_2S leads to a decrease in the HOMO–LUMO gap (E_g) values of $Be_{12}O_{12}$ and $Mg_{12}O_{12}$ by 3.84% and 17.54%, respectively, whereas the adsorption of SO_2 leads to a decrease in E_g values by 15.97% and 2.60%, respectively. At high temperatures, MD calculations declare that the $Be_{12}O_{12}$ and $Mg_{12}O_{12}$ nano-cages do not retain the H_2S on their surfaces, while SO_2 is retained at low and high temperatures. Moreover, the thermodynamic calculations show that the reactions between H_2S and SO_2 with $Be_{12}O_{12}$ and $Mg_{12}O_{12}$ nano-cages are exothermic. Furthermore, at the temperature range of 300–700 K, the H_2S reaction with $Mg_{12}O_{12}$ and $Be_{12}O_{12}$ is spontaneous and non-spontaneous, respectively, while the SO_2 reaction with $Mg_{12}O_{12}$ is spontaneous, whereas the SO_2 reaction with $Be_{12}O_{12}$ is spontaneous at temperatures up to 400 K. In addition, the reaction is capable to be reversed in the $H_2S/Mg_{12}O_{12}$ complex easier than in the $SO_2/Mg_{12}O_{12}$ complex.

Author Contributions: Conceptualization, K.M.E. and H.Y.A.; methodology, H.M.B., K.M.E. and H.Y.A.; software, H.Y.A.; formal analysis, H.M.B., K.M.E., S.B. and H.Y.A.; investigation, H.M.B., K.M.E., S.B. and H.Y.A. resources, H.M.B. and H.Y.A.; data curation, H.M.B., K.M.E. and H.Y.A.; writing—original draft preparation, H.M.B., K.M.E., S.B. and H.Y.A., writing—review and editing, H.M.B., K.M.E., S.B. and H.Y.A.; visualization, H.M.B., K.M.E., S.B. and H.Y.A.; supervision, K.M.E. and H.Y.A.; project administration, H.M.B.; funding acquisition, H.M.B. and H.Y.A. All authors have read and agreed to the published version of the manuscript.

Data Availability Statement: Not applicable.

Conflicts of Interest: The authors declare no conflict of interest.

References

1. Greenwood, N.N.; Earnshaw, A. *Chemistry of the Elements*, 2nd ed.; Butterworth Heinemann: Oxford, UK, 1998; ISBN 0-7506-3365-4.

2. Villalba, G.; Ayres, R.U. Schroder, Accounting for fluorine: Production, use, and loss. *J. Ind. Ecol.* **2008**, *11*, 85–101. https://doi.org/10.1162/jiec.2007.1075.

3. Zhang, X.X.; Gui, Y.G.; Dong, X.C. Preparation and application of TiO_2 nanotube array gas sensor for SF_6-insulated equipment detection: A review. *Nanoscale Res. Lett.* **2016**, *11*, 302. https://doi.org/10.1186/s11671-016-1516-4.

4. Gui, Y.G.; Tang, C.; Zhou, Q.; Xu, L.N.; Zhao, Z.Y.; Zhang, X.X. The sensing mechanism of N-doped SWCNTs toward SF_6 decomposition products: A first-principle study. *Appl. Surf. Sci.* **2018**, *440*, 846–852. https://doi.org/10.1016/j.apsusc.2018.01.247.

5. Ranea, V.A.; Quiña, P.L.D.; Yalet, N.M. General adsorption model for H_2S, H_2Se, H_2Te, NH_3, PH_3, AsH_3 and SbH_3 on the V_2O_5 (0 0 1) surface including the van der Waals interaction. *Chem. Phys. Lett.* **2019**, *720*, 58–63. https://doi.org/10.1016/j.cplett.2019.02.013.

6. Salih, E.; Ayesh, A.I. DFT investigation of H_2S adsorption on graphenenanosheets andnanoribbons: Comparative study. *Superlattices Microstruct.* **2020**, *146*, 106650. https://doi.org/10.1016/j.spmi.2020.106650.

7. Ganji, M.D.; Danesh, N. Adsorption of H_2S molecules by cucurbituril: An ab initio vdW-DF study. *RSC Adv.* **2013**, *3*, 22031–22038. https://doi.org/10.1039/C3RA41946K.

8. Faye, O.; Eduok, U.; Szpunar, J.; Samoura, A.; Beye, A. Beye, H_2S adsorption and dissociation on NH-decorated graphene: A first principles study. *Surf. Sci.* **2018**, *668*, 100–106. https://doi.org/10.1016/j.susc.2017.10.016.

9. Stern, A.C.; Boubel, R.W.; Turner, D.B.; Fox, D.L. *Fundamentals of Air Pollution*, 2nd ed.; Academic Press: Warsaw, Poland, 1997.

10. Eid, K.; Ammar, H. Adsorption of SO_2 on Li atoms deposited on MgO (1 0 0) surface: DFT calculations. *Appl. Surf. Sci.* **2011**, *257*, 6049–6058. https://doi.org/10.1016/j.apsusc.2011.01.122.

11. Li, L.; Moore, P. Putative biological roles of hydrogen sulfide in health and disease: A breath of not so fresh air? *Trends Pharmacol. Sci.* **2008**, *29*, 84–90. https://doi.org/10.1016/j.tips.2007.11.003. Epub 2008 Jan 3. PMID: 18180046.

12. Ayesh, A.I. H_2S and SO_2 adsorption on Cu doped MoSe2: DFT investigation. *Phys. Lett. A* **2021**, *422*, 127798. https://doi.org/10.1016/j.physleta.2021.127798.

13. Linn, W.S.; Avol, E.L.; Peng, R.-C.; Shamoo, D.A.; Hackney, J.D. Hackney, Replicated dose-response study of sulfur dioxide effects in normal, atopic, and asthmatic volunteers. *Am. Rev. Respir. Dis.* **1987**, *136*, 1127–1135. https://doi.org/10.1164/ajrccm/136.5.1127.

14. Noei, M. Different electronic sensitivity of BN and AlN nanoclusters to SO_2 gas: DFT studies. *Vacuum* **2016**, *135*, 44–49. https://doi.org/10.1016/j.vacuum.2016.10.029.

15. Salih, E.; Ayesh, A.I. CO, CO_2, and SO_2 detection based on functionalized graphene nanoribbons: First principles study. *Phys. E Low-Dimens. Syst. Nanostructures* **2020**, *123*, 114220. https://doi.org/10.1016/j.physe.2020.114220.

16. Salimifard, M.; Rad, A.S.; Mahanpoor, K. Mahanpoor, Surface interaction of H_2S, SO_2, and SO_3 on fullerene-like gallium nitride (GaN) nanostructure semiconductor. *Solid State Commun.* **2017**, *265*, 6–11. https://doi.org/10.1016/j.ssc.2017.07.018.

17. Sun, S.; Zhang, D.; Li, C.; Wang, Y. DFT study on the adsorption and dissociation of H_2S on CuO(111) surface. *RSC Adv.* **2015**, *5*, 21806–21811. https://doi.org/10.1039/c4ra16549g.

18. Zhang, H.; Cen, W.; Liu, J.; Guo, J.; Yin, H.; Ning, P. Adsorption and oxidation of SO_2 by graphene oxides: A van der Waals density functional theory study. *Appl. Surf. Sci.* **2015**, *324*, 61–67. https://doi.org/10.1016/j.apsusc.2014.10.087.

19. Barelli, L.; Bidini, G.; de Arespacochaga, N.; Pérez, L.; Sisani, E. Biogas use in high temperature fuel cells: Enhancement of KOH-KI activated carbon performance toward H_2S removal. *Int. J. Hydrogen Energy* **2017**, *42*, 10341–10353. https://doi.org/10.1016/j.ijhydene.2017.02.021.

20. Shi, L.; Yang, K.; Zhao, Q.; Wang, H.; Cui, Q. Characterization and mechanisms of H_2S and SO_2 adsorption by activated carbon, Energy Fuels. *Energy Fuels* **2015**, *29*, 6678–6685. https://doi.org/10.1021/acs.energyfuels.5b01696.

21. Nguyen-Thanh, D.; Bandosz, T.J. Effect of transition-metal cations on the adsorption of H_2S in modified pillared clays. *J. Phys. Chem. B* **2003**, *107*, 5812–5817. https://doi.org/10.1021/jp0223509.

22. Ozekmekci, M.; Salkic, G.; Fellah, M.F. Use of zeolites for the removal of H_2S: A mini-review. *Fuel Process. Technol.* **2015**, *139*, 49–60. https://doi.org/10.1016/j.fuproc.2015.08.015.

23. Albargi, H.; Ammar, H.Y.; Badran, H.M.; Algadi, H.; Umar, A. Umar, p-CuO/n-ZnO Heterojunction Structure for the Selective Detection of Hydrogen Sulphide and Sulphur Dioxide Gases: A Theoretical Approach. *Coatings* **2021**, *11*, 1200. https://doi.org/10.3390/coatings11101200.

24. Tang, Q.-L.; Duan, X.-X.; Zhang, T.-T.; Fan, X.; Zhang, X. Comparative theoretical study of the chemistry of hydrogen sulfide on Cu (100) and Au (100): Implications for sulfur tolerance of water gas shift nanocatalysts. *J. Phys. Chem. C* **2016**, *120*, 25351–25360. https://doi.org/10.1021/acs.jpcc.6b07050.

25. Chen, S.; Sun, S.; Lian, B.; Ma, Y.; Yan, Y.; Hu, S. The adsorption and dissociation of H_2S on Cu (100) surface: A DTF study. *Surf. Sci.* **2014**, *620*, 51–58. https://doi.org/10.1016/j.susc.2013.10.014.

26. Chen, H.; Pang, J.; Zhang, J.; Wei, G.; Wei, S.; Yan, J.; Jin, S. Exploring monolayer Janus MoSSe as potential gas sensor for Cl_2, H_2S and SO_2. *Comput. Theor. Chem.* **2022**, *1211*, 113665. https://doi.org/10.1016/j.comptc.2022.113665.

27. Siddique, S.A.; Sajid, H.; Gilani, M.A.; Ahmed, E.; Arshad, M.; Mahmood, T. Mahmood, Sensing of SO_3, SO_2, H_2S, NO_2 and N_2O toxic gases through aza-macrocycle via DFT calculations. *Comput. Theor. Chem.* **2022**, *1209*, 113606. https://doi.org/10.1016/j.comptc.2022.113606.

28. Cui, H.; Jiang, J.; Gao, C.; Dai, F.; An, J.; Wen, Z.; Liu, Y. DFT study of Cu-modified and Cu-embedded WSe_2 monolayers for cohesive adsorption of NO_2, SO_2, CO_2, and H_2S. *Appl. Surf. Sci.* **2022**, *583*, 152522. https://doi.org/10.1016/j.apsusc.2022.152522.

29. Korica, M.; Balić, I.; van Wyk, L.M.; van Heerden, D.P.; Nikolayenko, V.I.; Barbour, L.J.; Jednačak, T.; Đilović, I.; Balić, T. Inclusion of CO_2, NH_3, SO_2, Cl_2 and H_2S in porous N_4O_4-donor macrocyclic Schiff base. *Microporous Mesoporous Mater.* **2022**, *332*, 111708. https://doi.org/10.1016/j.micromeso.2022.111708.

30. Eid, K.; Ammar, H. A density functional study of NO_2 adsorption on perfect and defective MgO (100) and Li/MgO (100) surfaces. *Appl. Surf. Sci.* **2012**, *258*, 7689–7698. https://doi.org/10.1016/j.apsusc.2012.04.124.

31. Ammar, H.; Eid, K. NO_2 interaction with Au atom adsorbed on perfect and defective MgO(100) surfaces: Density functional theory calculations. *J. Nanosci. Nanotechnol.* **2013**, *13*, 6660–6671. https://doi.org/10.1166/jnn.2013.7760.

32. Eid, K.; Taha, H.; Kamel, M.; Ashour, A.; Halim, W.A. Abdel Halim, DFT calculations of the CO adsorption on Mn, Fe, Co, and Au deposited at MgO (1 0 0) and CdO (1 0 0). *Appl. Surf. Sci.* **2012**, *258*, 9876–9890. https://doi.org/10.1016/j.apsusc.2012.06.045.

33. Eid, K.; Matlak, M.; Zieliński, J. Apex oxygen and effective pairing interaction among planar oxygen quasiparticles in copper oxide superconductors. *Phys. C Supercond.* **1994**, *220*, 61–66. https://doi.org/10.1016/0921-4534(94)90884-2.

34. Ammar, H.Y.; Badran, H.M.; Umar, A.; Fouad, H.; Alothman, O.Y. ZnO Nanocrystal-Based Chloroform Detection: Density Functional Theory (DFT) Study. *Coatings* **2019**, *9*, 769. https://doi.org/10.3390/coatings9110769.

35. Fadradi, M.A.; Movlarooy, T. Ab initio study of adsorption of CO on BNNTs: For gas nanosensor applications. *Mater. Chem. Phys.* **2018**, *215*, 360–367https://doi.org/10.1016/j.matchemphys.2018.04.102.

36. Sun, Y.F.; Liu, S.B.; Meng, F.L.; Liu, J.Y.; Jin, Z.; Kong, L.T.; Liu, J.H. Metal oxide nanostructures and their gas sensing properties: A review. *Sensors* **2012**, *12*, 2610–2631. https://doi.org/10.3390/s120302610.

37. Ammar, H.; Eid, K.; Badran, H. Interaction and detection of formaldehyde on pristine and doped boron nitride nano-cage: DFT calculations. *Mater. Today Commun.* **2020**, *25*, 101408. https://doi.org/10.1016/j.mtcomm.2020.101408.

38. Shamlouei, H.R.; Nouri, A.; Mohammadi, A.; Tehrani, A.D. Influence of transition metal atoms doping on structural, electronic and nonlinear optical properties of $Mg_{12}O_{12}$ nanoclusters: A DFT study. *Phys. E* **2016**, *77*, 48–53. https://doi.org/10.1016/j.physe.2015.10.035.

39. Ren, L.; Cheng, L.; Feng, Y.; Wang, X. Geometric and electronic structures of $(BeO)_N$ (N = 2–12, 16, 20, and 24): Rings, double rings, and cages. *J. Chem. Phys.* **2012**, *137*, 014309. https://doi.org/10.1063/1.4731808.

40. Ziemann, P.J.; Castleman, A.W., Jr. Stabilities and structures of gas phase MgO clusters. *J. Chem. Phys.* **1991**, *94*, 718–728. https://doi.org/10.1063/1.460340.

41. Lenglet, M. Iono-covalent character of the metal oxygen bonds in oxides: A comparison of experimental and theoretical data. *Act. Passiv. Electron. Compon.* **2004**, *27*, 1–60. https://doi.org/10.1080/08827510310001116142.

42. Hwang, D.Y.; Mebel, A.M. Theoretical study of the reaction of beryllium oxide with methane. *Chem. Phys. Lett.* **2001**, *348*, 303–310. https://doi.org/10.1016/S0009-2614(01)01120-4.

43. Jouypazadeh, H.; Farrokhpour, H. DFT and TD-DFT study of the adsorption and detection of sulfur mustard chemical warfare agent by the C_{24}, $C_{12}Si_{12}$, $Al_{12}N_{12}$, $Al_{12}P_{12}$, $Be_{12}O_{12}$, $B_{12}N_{12}$ and $Mg_{12}O_{12}$ nanocages. *J. Mol. Struct.* **2018**, *1164*, 227–238. https://doi.org/10.1016/j.molstruc.2018.03.051.

44. Rezaei-Sameti, M.; Abdoli, S. The capability of the pristine and (Sc, Ti) doped $Be_{12}O_{12}$ nanocluster to detect and adsorb of Mercaptopyridine molecule: A first principle study. *J. Mol. Struct.* **2019**, *1205*, 127593. https://doi.org/10.1016/j.molstruc.2019.127593.

45. Ahangari, M.G.; Mashhadzadeh, A.H. Dynamics study on hydrogen storage capacity of C_{24}, $B_{12}N_{12}$, $Al_{12}N_{12}$, $Be_{12}O_{12}$, $Mg_{12}O_{12}$, and $Zn_{12}O_{12}$ nano-cages. *Int. J. Hydrogen Energy* **2020**, *45*, 6745–6756. https://doi.org/10.1016/j.ijhydene.2019.12.106.

46. Ammar, H.; Eid, K.; Badran, H. TM-doped $Mg_{12}O_{12}$ nano-cages for hydrogen storage applications:Theoretical study. *Results Phys.* **2022**, *35*, 105349https://doi.org/10.1016/j.rinp.2022.105349.

47. Fallahi, P.; Jouypazadeh, H.; Farrokhpour, H. Theoretical studies on the potentials of some nanocages ($Al_{12}N_{12}$, $Al_{12}P_{12}$, $B_{12}N_{12}$, $Be_{12}O_{12}$, $C_{12}Si_{12}$, $Mg_{12}O_{12}$ and C_{24}) on the detection and adsorption of Tabun molecule: DFT and TD-DFT study. *J. Mol. Liq.* **2018**, *260*, 138–148. https://doi.org/10.1016/j.molliq.2018.03.085.

48. Kohn, W.; Sham, L.J. Self-consistent equations including exchange and correlation effects. *Phys. Rev. A* **1965**, *140*, **A1133–A1138**. https://doi.org/10.1103/PhysRev.140.A1133.

49. Grimme, S.; Antony, J.; Ehrlich, S.; Krieg, H. A consistent and accurate ab initio parametrization of density functional dispersion correction (DFT-D) for the 94 elements H-Pu. *J. Chem. Phys.* **2010**, *132*, **154104–154119**. https://doi.org/10.1063/1.3382344.

50. Becke, A.D. Density-functional thermochemistry. III. The role of exact exchange. *J. Chem. Phys.* **1993**, *98*, **5648–5652**. https://doi.org/10.1063/1.464913.

51. Lee, C.; Yang, W.; Parr, R.G. Development of the Colle-Salvetti correlation-energy formula into a functional of the electron density. *Phys. Rev. B* **1988**, *37*, **785–789**. https://doi.org/10.1103/PhysRevB.37.785.

52. Miehlich, B.; Savin, A.; Stoll, H.; Preuss, H. Preuss, Results obtained with the correlation-energy density functionals of Becke and Lee, Yang and Parr. *Chem. Phys. Lett.* **1989**, *157*, 200–206. https://doi.org/10.1016/0009-2614(89)87234-3.

53. Pearson, R.G. Absolute electronegativity and hardness correlated with molecular orbital theory. *Proc. Natl. Acad. Sci. USA* **1986**, *83*, 8440–8441. https://doi.org/10.1073/pnas.83.22.8440.

54. Parr, R.G.; Szentpály, L.V.; Liu, S. Electrophilicity, index. *J. Am. Chem. Soc.* **1999**, *121*, 1922–1924. https://doi.org/10.1021/ja983494x.

55. Boys, S.F.; Bernardi, F.D. The calculation of small molecular interactions by the differences of separate total energies. Some procedures with reduced errors. *Mol. Phys.* **1970**, *19*, 553–566. https://doi.org/10.1080/00268977000101561.

56. Guo, C.; Wang, C. A theoretical study on cage-like clusters (C_{12}-Ti_6 and C_{12}-Ti_6^{+2}) for dihydrogen storage. *Int. J. Hydrogen Energy* **2019**, *44*, 10763–10769. https://doi.org/10.1016/j.ijhydene.2019.02.212.

57. Frisch, M.; Trucks, G.; Schlegel, H.; Scuseria, G.; Robb, M.; Cheeseman, J.; Scalmani, G.; Barone, V.; Mennucci, B.; Petersson, G. *Gaussian 09, Revision D.01*; Gaussian, Inc.: Wallingford, CT, USA, 2009.

58. O'Boyle, N.M.; Tenderholt, A.L.; Langner, K.M. Cclib: A library for package-independent computational chemistry algorithms. *J. Comput. Chem.* **2008**, *29*, 839–845. https://doi.org/10.1002/jcc.20823.

59. Glendening, E.D.; Reed, A.E.; Carpenter, J.E.; Weinhold, F. *NBO Version 3.1.*; Gaussian, Inc.: Wallingford, CT, USA, 2003.

60. Sajid, H; Siddique, S.A.; Ahmed, E.; Arshad, M.; Gilani, M.A.; Abdul Rauf; Imran M.; Mahmood, F. DFT outcome for comparative analysis of $Be_{12}O_{12}$, $Mg_{12}O_{12}$ and $Ca_{12}O_{12}$ nanocages toward sensing of N_2O, NO_2, NO, H_2S, SO_2 and SO_3 gases. Comput. Theor. Chem. **2022**, 1211, 113694. https://doi.org/10.1016/j.comptc.2022.113694

61. Shakerzdeh, E.; Tahmasebi, E.; Shamlouei, H.R. Shamlouei, The influence of alkali metals (Li, Na and K) interaction with $Be_{12}O_{12}$ and $Mg_{12}O_{12}$ nanoclusters on their structural, electronic and nonlinear optical properties: A theoretical study. *Synth. Met.* **2015**, *204*, 17–24. https://doi.org/10.1016/j.synthmet.2015.03.008.

62. Kakemam, J.; Peyghan, A.A. Electronic, energetic, and structural properties of C- and Si-doped $Mg_{12}O_{12}$ nano-cages. *Comput. Mater. Sci.* **2013**, *79*, 352–355. https://doi.org/10.1016/j.commatsci.2013.06.036.

63. El-Gharkawy, E.-S.R.H.; Ammar, H. Adsorption of CO on TM-Deposited $(MgO)_{12}$ Nano-Cage (TM = Ni, Pd and Pt): A Study on Electronic Properties. *J. Nanoelectron. Optoelectron.* **2018**, *13*, 546–553. https://doi.org/10.1166/jno.2018.2163.

64. Ammar, H.; Badran, H.; Eid, K. TM-doped $B_{12}N_{12}$ nano-cage (TM = Mn, Fe) as a sensor for CO, NO, and NH_3 gases: A DFT and TD-DFT study. *Mater. Today Commun.* **2020**, *25*, 101681. https://doi.org/10.1016/j.mtcomm.2020.101681.

65. Yang, M.; Zhang, Y.; Huang, S.; Liu, H.; Wang, P.; Tian, H. Theoretical investigation of CO adsorption on TM-doped $(MgO)_{12}$ (TM = Ni, Pd, Pt) nanotubes. *Appl. Surf. Sci.* **2011**, *258*, 1429–1436. https://doi.org/10.1016/j.apsusc.2011.09.097.

66. Abbasi, M.; Nemati-Kande, E.; Mohammadi, M.D. Doping of the first row transition metals onto $B_{12}N_{12}$ nanocage: A DFT study. *Comput. Theor. Chem.* **2018**, *1132*, 1–11. https://doi.org/10.1016/j.comptc.2018.04.003.

67. Ammar, H.; Eid, K.; Badran, H. The impact of an external electric field on methanol adsorption on $XB_{11}N_{12}$ (X = B, Co, Ni) nano-cages: A DFT and TD-DFT study. *J. Phys. Chem. Solids* **2021**, *153*, 110033. https://doi.org/10.1016/j.jpcs.2021.110033.

68. Alam, M.S.; Lee, D.U. Molecular structure, spectral (FT-IR, FT-Raman, Uv-Vis, and fluorescent) properties and quantum chemical analyses of azomethine derivative of 4-aminoantipyrine. *J. Mol. Struct.* **2020**, *1227*, 129512. https://doi.org/10.1016/j.molstruc.2020.129512.

69. Balan, C.; Pop, L.-C.; Baia, M. IR, Raman and SERS analysis of amikacin combined with DFT-based calculations, Spectrochimica. *Acta Part A Mol. Biomol. Spectrosc.* **2019**, *214*, 79–85https://doi.org/10.1016/j.saa.2019.02.012.

70. Yüksel, B. Spectroscopic characterization (IR and NMR), structural investigation, DFT study, and Hirshfeld surface analysis of two zinc(II) 2-acetylthiophenyl-thiosemicarbazone complexes. *J. Mol. Struct.* **2020**, *1229*, 129617. https://doi.org/10.1016/j.molstruc.2020.129617.

71. Badran, H.; Eid, K.; Ammar, H. DFT and TD-DFT studies of halogens adsorption on cobalt-doped porphyrin: Effect of the external electric field. *Results Phys.* **2021**, *23*, 103964. https://doi.org/10.1016/j.rinp.2021.103964.

72. Kittel, C. *Introduction to Solid State Physics*; John Wiley and Sons: Hoboken, NJ, USA, 2005; pp. 216–226.

73. Kasap, S.O. *Principles of Electronic Materials and Devices*; McGraw-Hill: Boston, MA, USA, 2006; pp. 378–405.

74. Ammar, H.; Badran, H. Effect of CO adsorption on properties of transition metal doped porphyrin: A DFT and TD-DFT study. *Heliyon* **2019**, *5*, e02545. https://doi.org/10.1016/j.heliyon.2019.e02545.

75. Guo, J.; Guan, L.; Wang, S.; Zhao, Q.; Wang, Y.; Liu, B. Study of hydrogen adsorption on the Ti (0 0 0 1)-(1 × 1) surface by density functional theory. *Appl. Surf. Sci.* **2008**, *255*, 3164–3169. https://doi.org/10.1016/j.apsusc.2008.09.006.

76. Jigang, W.; Ji, L.; Yong, D.; Yan, Z.; Lihui, M.; Asadi, H. Effect of platinum on the sensing performance of ZnO nanocluster to CO gas. *Solid State Commun.* **2020**, *316-317*, 113954. https://doi.org/10.1016/j.ssc.2020.113954.

77. Sconza, A.; Torzo, G. An undergraduate laboratory experiment for measuring the energy gap in semiconductors. *Eur. J. Phys.* **1989**, *10*, 123–126. https://doi.org/10.1088/0143-0807/10/2/009.

78. Demir, S.; Fellah, M.F. A DFT study on Pt doped (4,0) SWCNT: CO adsorption and sensing. *Appl. Surf. Sci.* **2019**, *504*, 144141. https://doi.org/10.1016/j.apsusc.2019.144141.

79. Cui, H.; Zhang, G.; Zhang, X.; Tang, J. Rh-doped $MoSe_2$ as a toxic gas scavenger: A first-principles study. *Nanoscale Adv.* **2018**, *1*, 772–780. https://doi.org/10.1039/c8na00233a.

80. Segall, M.D.; Shah, R.; Pickard, C.J.; Payne, M.C. Population analysis of plane-wave electronic structure calculations of bulk materials. *Phys. Rev. B* **1996**, *54*, 16317–16320. https://doi.org/10.1103/PhysRevB.54.16317.